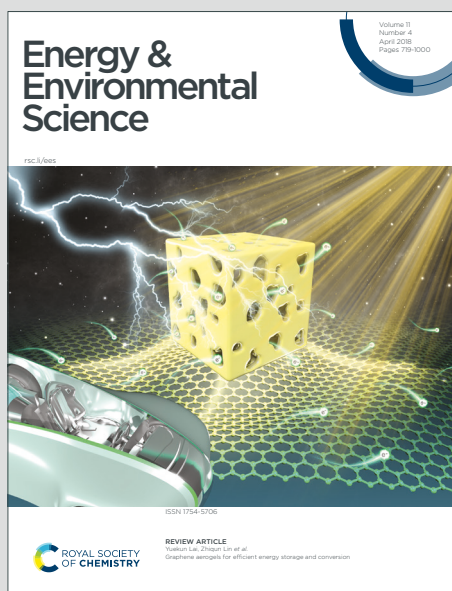


# Energy & Environmental Science

Accepted Manuscript

This article can be cited before page numbers have been issued, to do this please use: G. Ding, C. Li, L. Chen and G. Liao, *Energy Environ. Sci.*, 2024, DOI: 10.1039/D4EE01748J.



This is an Accepted Manuscript, which has been through the Royal Society of Chemistry peer review process and has been accepted for publication.

Accepted Manuscripts are published online shortly after acceptance, before technical editing, formatting and proof reading. Using this free service, authors can make their results available to the community, in citable form, before we publish the edited article. We will replace this Accepted Manuscript with the edited and formatted Advance Article as soon as it is available.

You can find more information about Accepted Manuscripts in the [Information for Authors](#).

Please note that technical editing may introduce minor changes to the text and/or graphics, which may alter content. The journal's standard [Terms & Conditions](#) and the [Ethical guidelines](#) still apply. In no event shall the Royal Society of Chemistry be held responsible for any errors or omissions in this Accepted Manuscript or any consequences arising from the use of any information it contains.

**Broader Context**

The technology of photo(electro)catalytic reduction of CO<sub>2</sub> aims to mimic the natural photosynthesis mechanism by using light or electrical energy to convert excess CO<sub>2</sub> in the atmosphere into valuable chemicals like C<sub>1</sub>, C<sub>2</sub>, and other hydrocarbons. This process helps in efficiently utilizing carbon resources and reducing greenhouse gas emissions. Porphyrin-based metal-organic frameworks (MOFs) has attracted much attention in the field of CO<sub>2</sub> photo(electro)reduction, such as superior CO<sub>2</sub> adsorption due to their many advantages such as tunable photoelectrochemical properties, strong light absorption and response abilities, large specific surface area, and abundant and evenly distributed active sites. This review presents a panorama of the latest developments of the emerging porphyrin-based MOFs photo(electro)catalysts for CO<sub>2</sub> reduction. It starts with the synthesis and design of porphyrin-based MOFs. After that, the basic principle for CO<sub>2</sub> reduction is also illustrated. Later, the recent advancements have been made in the field of porphyrin-based MOFs for applications in photo(electron)catalytic CO<sub>2</sub> reduction are exemplified. In the end, this review also offers some new views into the major challenges, opportunities, and heuristic perspectives for future researches in this emerging field.

# Emerging porphyrin-based metal-organic frameworks for photo(electro)catalytic CO<sub>2</sub> reduction

View Article Online  
DOI: 10.1039/D4EE01748J

Guixiang Ding<sup>a,1</sup>, Chunxue Li<sup>b,1</sup>, Lihui Chen<sup>a</sup>, and Guangfu Liao<sup>a,\*</sup>

<sup>a</sup>National Forestry and Grassland Administration Key Laboratory of Plant Fiber Functional Materials, College of Materials Engineering, Fujian Agriculture and Forestry University, Fuzhou 350002, China.

<sup>b</sup>College of Ecological Environment and Urban Construction, Fujian University of Technology, Fuzhou 350118, China.

<sup>1</sup>These authors contributed equally to this work.

\*Correspondence: [liaogf@mail2.sysu.edu.cn](mailto:liaogf@mail2.sysu.edu.cn) (G. Liao).

**Abstract:** Amidst the significant challenges posed by global climate change and the need for sustainable resource recycling, there is a pressing demand for the development of new materials that offer high cost-effectiveness, exceptional conversion efficiency, and robust stability to facilitate the conversion of CO<sub>2</sub> into high-value products. Metal-organic frameworks (MOFs), which incorporate versatile porphyrin fragments, have emerged as promising candidates in the realm of photo(electro)catalytic CO<sub>2</sub> reduction. Noteworthy for their straightforward synthesis, tunable structure, chemical stability, and abundance of active sites, MOFs enriched with specific functional porphyrins can be precisely incorporated through *in-situ* self-assembly or post-synthesis techniques, thereby broadening the scope of design possibilities for porphyrin-based MOFs. This comprehensive review delves into the rational design principles and recent advancements in the utilization of porphyrin-based MOFs for photo(electro)catalytic CO<sub>2</sub> reduction. It elucidates the synthesis methods, CO<sub>2</sub> interaction mechanisms, and delves into the latest research endeavors encompassing catalyst structure optimization, activity enhancement, selectivity control, and other pivotal breakthroughs. Furthermore, it conducts a detailed analysis of the current technical challenges, future trends, and the promising prospects of porphyrin-based MOFs in driving the industrialization of this technology. By offering a thorough theoretical framework and practical insights, this review serves as a valuable resource for enhancing the understanding and application of porphyrin-based MOFs in high-value CO<sub>2</sub> conversion, thereby paving the way for improved catalytic performance and the successful implementation of this technology.

**Keywords:** Porphyrin-based MOFs; Photocatalysis; Electrocatalysis; CO<sub>2</sub> conversion

### Broader Context

The technology of photo(electro)catalytic reduction of CO<sub>2</sub> aims to mimic the natural photosynthesis mechanism by using light or electrical energy to convert excess CO<sub>2</sub> in the atmosphere into valuable chemicals like C<sub>1</sub>, C<sub>2</sub>, and other hydrocarbons. This process helps in efficiently utilizing carbon resources and reducing greenhouse gas emissions. Porphyrin-based metal-organic frameworks (MOFs) has attracted much attention in the field of CO<sub>2</sub> photo(electro)reduction, such as superior CO<sub>2</sub> adsorption due to their many advantages such as tunable photoelectrochemical properties, strong light absorption and response abilities, large specific surface area, and abundant and evenly distributed active sites. This review presents a panorama of the latest developments of the emerging porphyrin-based MOFs photo(electro)catalysts for CO<sub>2</sub> reduction. It starts with the synthesis and design of porphyrin-based MOFs. After that, the basic principle for CO<sub>2</sub> reduction is also illustrated. Later, the recent advancements have been made in the field of porphyrin-based MOFs for applications in photo(electron)catalytic CO<sub>2</sub> reduction are exemplified. In the end, this review also offers some new views into the major challenges, opportunities, and heuristic perspectives for future researches in this emerging field.

## 1. Introduction

The greenhouse effect caused by excessive CO<sub>2</sub> emissions has emerged as a significant threat to human survival.<sup>1-5</sup> The conversion of CO<sub>2</sub> into energy is an effective strategy that addresses two issues simultaneously: protecting the environment and conserving non-renewable energy sources.<sup>6-8</sup> Among different approaches to CO<sub>2</sub> energy conversion, photo(electro)catalytic CO<sub>2</sub> reduction has gained considerable attention.<sup>9-11</sup> This method offers favorable reaction conditions and enables the production of fuels and chemicals, thereby mitigating the environmental impact of excessive CO<sub>2</sub> emissions.<sup>12</sup> However, symmetric linear CO<sub>2</sub> molecular structure means process of activation and transformation requires more input energy and lower overpotential to overcome the sluggish reaction kinetics.<sup>13, 14</sup> For photocatalytic CO<sub>2</sub> reduction, appropriate conduction band potential and effective chemisorption are desirable in photocatalysts.<sup>15</sup> However, low carrier separation efficiency and poor electron conductivity limit the photocatalytic activity.<sup>16, 17</sup> Numerous reports have suggested various approaches to enhance the photocatalytic activity, which can be broadly categorized as: structural engineering (doping element,<sup>18-20</sup> defect engineering,<sup>21-23</sup> etc) and co-catalytic design (heterojunction,<sup>24-27</sup> loading noble metal,<sup>28, 29</sup> single atom catalysis,<sup>30, 31</sup> etc). On the other hand, for electrochemical CO<sub>2</sub> reduction reaction (CO<sub>2</sub>RR), electrocatalysts are expected to have lower overpotential and higher efficiency in CO<sub>2</sub>RR.<sup>32</sup> However, the hydrogen evolution reaction (HER) competes with CO<sub>2</sub>RR in aqueous systems, as HER occurs in a similar potential range.<sup>33-35</sup> Additionally, the multi-electron and multi-proton reactions also reduce the selectivity of CO<sub>2</sub>RR, making it satisfactory. Both structure engineering and surface decoration are key approaches to enhance the selectivity and catalytic activity of electrocatalysts. It's important to note that selecting the right photo(electro)catalytic materials is also crucial for optimizing selectivity and maintaining high performance in catalytic CO<sub>2</sub> reduction.

Recently, the research of metal-organic frameworks (MOFs) about the field of energy conversion of CO<sub>2</sub> has become a hot discussion and more scientific achievements have been published in some top journals.<sup>36, 37</sup> As we know, MOFs are a class of porous crystal materials consist of inorganic metal ions or clusters and organic linkers.<sup>38-40</sup> The notion of MOFs was first introduced by Yaghi et al. in 1995.<sup>41</sup> With thorough research on the properties and synthesis strategies of MOFs, more outstanding merits have been discovered for their applications in the field of energy conversion, gas storage, separation, and sensors.<sup>42, 43</sup> These merits can be attributed to their large special surface area, tunable open channels, and abundant active sites.<sup>44</sup> In addition, the flexible composition of metal nodes and the organic linkers in MOFs materials allows for excellent functional expansion and regulation.<sup>45-48</sup> Thus, MOFs have long been considered as a promising platform to be induced in the research and application of energy conversion of CO<sub>2</sub>.<sup>49</sup>

Porphyryns are widespread in nature and play an irreplaceable role in the metabolism of life, such as, participating in photosynthesis as chlorophyll, being involved in the transportation of oxygen in the blood in the form of hemoglobin and

producing vitamin B<sub>12</sub> of red blood cell, etc.<sup>50-53</sup> In case of the structure, porphyrins are a class of aromatic organics with macrocyclic conjugated planar structures, the central compound is a porphyrin core of 18- $\pi$  conjugate electrons, and substituents are observed on the bridging hypomethyl (=CH<sub>2</sub>-) groups.<sup>54</sup> Meanwhile, nitrogen atoms existing on porphine can coordinate with most metal ions, ultimately, porphyrins transform into metalloporphyrins.<sup>55-57</sup> Porphyrin materials assume the active centers in diverse bioenzymatic catalysts and environmentally friendly biomimetic catalysts, and show outstanding performance and superior selectivity in catalytic reaction.<sup>41, 58-60</sup> Noteworthy, metalloporphyrins present stronger catalytic and photoelectric activity than porphyrins, which mainly attributes to the fact that the addition of the coordinating metal ions change the configuration of electrons in porphyrins.<sup>56, 61, 62</sup> With the increasing research on porphyrins and porphyrin derivative for photo(electro)catalytic application, more drawbacks, such as, small specific surface area, non-recyclable for homogeneous system, low catalytic efficiency are exposed during the catalytic process.<sup>63-65</sup> In this case, the strategy that integration of porphyrins and porphyrin derivatives into MOFs has received highly attention in the field of photo(electro)catalytic CO<sub>2</sub> reduction. In addition, porphyrin MOFs stand out with excellent light absorption and precise active center, facilitating tailored design and exhibiting great potential in advanced photo(electro)catalytic applications compared to conventional MOFs.

Over the past few years, the emerging porphyrin-based MOFs have been widely reported for photo(electro)catalytic CO<sub>2</sub> reduction. It is an opportune moment to offer a review on porphyrin-based MOFs for photo(electro)catalytic CO<sub>2</sub> reduction. Up to now, although there have been many inspiring reviews on porphyrin-based MOFs for various applications,<sup>66-72</sup> a comprehensive review focusing on porphyrin-based MOFs for photo(electro)catalytic CO<sub>2</sub> reduction is inexistent. In this review, the synthetic approaches of porphyrin-based MOFs and basic principle for CO<sub>2</sub> reduction are firstly exhibited. Subsequently, the recent advancements in the utilization of porphyrin-based MOFs in photo(electro)catalytic CO<sub>2</sub> reduction are outlined. Lastly, the challenges and prospects of this class of emerging materials for the application of photo(electro)catalytic CO<sub>2</sub> reduction are discussed.

## 2. Synthesis and design of porphyrin-based MOFs

A diverse set of MOFs, such as, zeolite imidazolate frameworks (ZIFs)<sup>73-75</sup>, isoreticular metal-organic frameworks (IRMOFs),<sup>76</sup> material soffitute lavoisierframeworks (MILs),<sup>55</sup> ocket-channel frameworks (PCNs)<sup>77</sup> have been successfully designed and synthesized. According to the past experiences, the development trend of the synthesis and design of porphyrin-based MOFs generally follows the MOFs guideline. Toward the target of pragmatization, the design and synthesis of porphyrin-based MOFs meet the characteristics of excellent photo(electro)chemical property and chemical stability. Meanwhile, combined with the porous and large specific surface area of the framework structure of MOFs, this enables the development of porphyrin-based MOFs in CO<sub>2</sub> capture with great

potential. As research on the application of porphyrin-based MOFs in CO<sub>2</sub> catalysis advances, numerous design concepts and structural engineering approaches for porphyrin-based MOFs have been proposed. These concepts have been thoroughly validated, demonstrating their excellent catalytic activities. The synthesis, construction, and development of porphyrin-based MOFs have been described in recent years through two design directions, namely porphyrinic MOFs and porphyrin@MOFs.

View Article Online  
DOI: 10.1039/D4EE01748J

## 2.1. Porphyrinic MOFs

Porphyrins are heterocyclic macromolecular compounds that can act as functional organic linkers and coordinate with metal ions or secondary building units (SBUs) to form porphyrinic MOFs, the secondary building units (SBUs) refer to the fundamental repeating units that constitute the crystalline structure of porphyrinic MOFs. These units typically arise from the coordination between metal ions (such as zinc, copper, iron, etc.) and organic ligands (commonly carboxylic acids, imidazoles, bipyridines, etc.), forming simpler polyhedral structures. Acting as building blocks, SBUs assemble into larger and more intricate three-dimensional networks through various connecting modes, including vertex-sharing or edge-sharing, to create the complex architectures of porphyrinic MOFs, common secondary building units include octahedral structures formed by four metal ions and six organic ligands, denoted as  $[M_4(O/R)_6]$ , where M represents metal ions, and O or R signifies oxygen atoms or functional groups within the organic ligands, metal nodes and SBUs have significant influences on the structural and physicochemical properties of porphyrinic MOFs.<sup>44, 60</sup> Some common porphyrin linkers are shown in **Fig. 1b**. In addition, porphyrinic MOFs can also be further enhanced by incorporating other functionalized components, such as quantum dots and photoelectronic nanoparticles. This modification transforms it into an exceptionally advanced photoelectrocatalytic platform. Besides composition, the structure of porphyrinic MOFs is crucial in the field of energy-conversion catalysis<sup>78-80</sup>. In this section, we introduce the synthesis strategy of porphyrinic MOFs from topological engineering, metal-organic cage engineering and pillar-layer engineering. Meanwhile, the structural stability of porphyrinic MOFs with different synthetic ideas is elaborated.



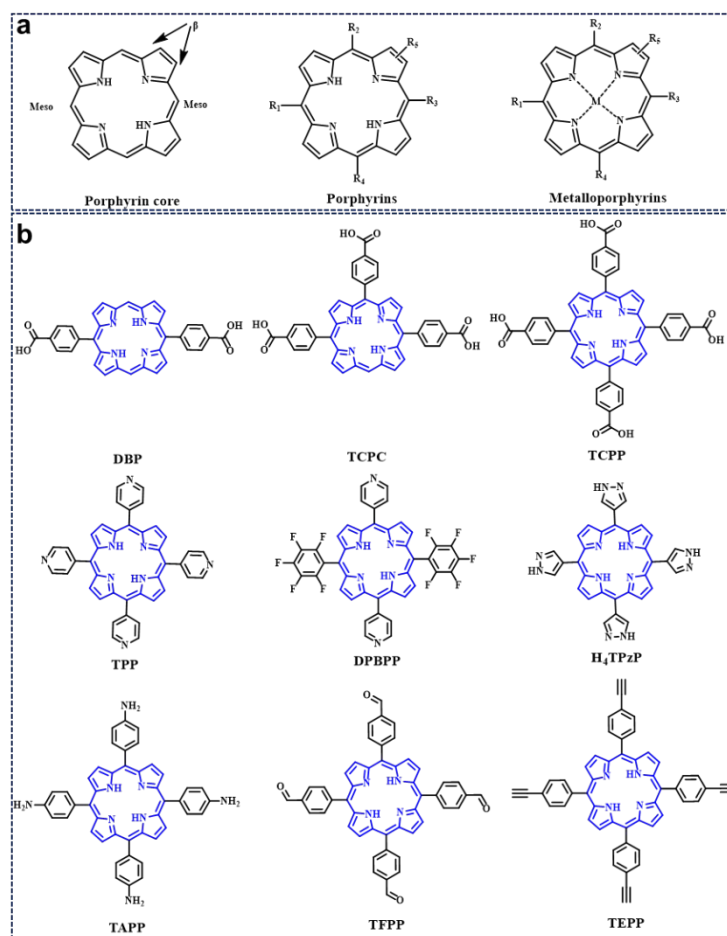


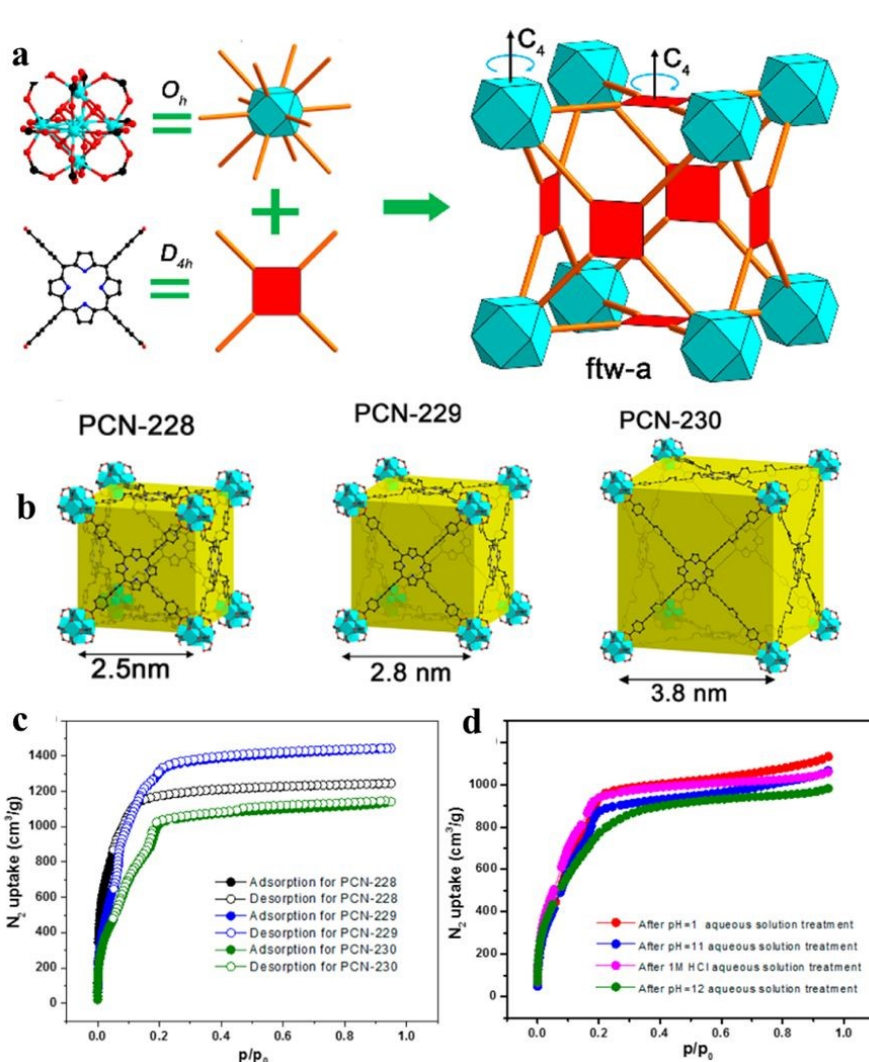
**Fig. 1.** (a) Representative molecular structures of Structure diagrams of porphyrin core, porphyrins, metalloporphyrins. (b) Porphyrin-based organic linkers for the synthesis of porphyrin-based MOFs.

### 2.1.1. Topological engineering

Topology is a fundamental branch of mathematics that studies the properties of space that remain unchanged under continuous deformation. In other words, topology is concerned with the "connectivity" and "hollowness" of objects rather than their specific shape, size or distance. Similarly in chemical synthesis, topological strategies emphasize "connectivity" and "adjacency" without concerning themselves with precise distances or directions. This approach focuses on the relationship between points, which represent entities like atoms or vertices, and lines that symbolize connections such as chemical bonds or edges. In the design and synthesis of porphyrinic MOFs, topological strategies can employ a variety of topological indices to guide synthetic routes, predict structural characteristics, and optimize material properties. Such as, the connectivity index measures the degree of connection among atoms or structural units within a molecule, aiding in the understanding of porosity and diffusion properties in porphyrinic MOFs, the vertex degree reflects the local density and potential coordination patterns within a structure, analysis of ring count and size distribution, which examines the presence of various-sized rings within a

molecule, provides guidance for predicting the stability and functionalization pathways of porphyrinic MOFs. In short, topological engineering facilitates the simplification and analysis of complex porphyrin-based MOF structures, providing guidance for structural design and synthesis. Currently, a prevalent topological strategy involves maintaining the inherent topology during the construction of porphyrinic MOFs, ensuring structural integrity and intended functionality.<sup>49, 81, 82</sup> This process alters the structure, lengths of porphyrin-organic linkers, and metal nodes in the framework, facilitating the functionalized synthesis of porphyrinic MOFs.<sup>75, 83</sup> The advancement of topological engineering has significantly enhanced the utility of porphyrinic MOFs for energy conversion applications. For example, pore size in porphyrinic MOFs can be adjusted by modifying linker lengths.<sup>84, 85</sup> Furthermore, changing the coordination metal in the porphyrin core allows for modification of the photoelectric properties of porphyrinic MOFs. Additionally, enhancing the stability of porphyrinic MOFs can be achieved by adjusting bond lengths and angles of centers and ligands through altering metal clusters or metal nodes.

As shown in **Fig. 1**, porphyrin consists of a central heterocyclic ring and external functional groups, the structure and length of these functional groups can be easily modified. Thus, porphyrin function as linkers usually with a large size about 2.5 nm, which facilitates the generation of large pores inside the organic framework, ultimately forming mesoporous porphyrinic MOFs materials. Here, Zhou<sup>86</sup> and his group developed a series of porphyrinic MOFs consist of tetratopic carboxylate porphyrin ligand H<sub>4</sub>TCPP (tetrakis (4-carboxyphenyl)-porphyrin) with D<sub>4h</sub> symmetry and the 12-connected Zr<sub>6</sub> cluster with O<sub>h</sub> symmetry, topological connection of those two nodes to each other could ideally give rise to a highly connected ftw-a network (**Fig. 2a**). Herein, the desired formation of organic linkers were elongated through arranging the vicinal phenyl ring and carboxylate group. Ultimately, a series of mesoporous porphyrinic MOFs with ftw-a topology, namely PCN-228, PCN-229, and PCN-230 (PCN is the abbreviation of porous coordination network) were synthesized by the assembly of organic linkers and 12-connected Zr<sub>6</sub> cluster. The mesopores size of porphyrinic MOFs (PCN-228, PCN-229, and PCN-230) were 2.5, 2.8, 3.8 nm, respectively (**Fig. 2b**), and PCN-229 present the most special surface area according to Brunauer-Emmett-Teller (BET) test (**Fig. 2c**). Longer linker possible lower stability, however, PCN-230 showed unexpected stability over the pH range of 0-12 in aqueous solution, which demonstrated PCN-230's excellent PH tolerance and chemical stability (**Fig. 2d**). The adjustment of linker length in porphyrin-based MOFs is expected to broaden their application potential, particularly in gas adsorption and catalytic site distribution. This modification will help overcome stability issues, enhancing the versatility and feasibility of their use.



View Article Online  
DOI: 10.1039/D4EE01748J

**Fig. 2.** (a) Assembly of  $O_h$  and  $D_{4h}$  nodes into ftw-a network. (b) Structures and crystals of PCN-230. (c-d)  $N_2$  adsorption isotherms of PCN-230 after different treatment. Reproduced from ref. <sup>86</sup>.

Copyright 2022 ACS.

Then, the interaction between metal nodes and porphyrinic linkers plays a crucial role in the chemical stabilization of porphyrinic MOFs. By adjusting the hardness of metal ions and porphyrin ligands, the chemical stability of porphyrinic MOFs can be controlled in accordance with the soft and hard acid-base theory (HSAB).<sup>87</sup> Especially, porphyrinic MOFs consist of coordination centers with high-valent metal ions and linkers with carboxylate terminal group exhibit a significant degree of variability when exposed to water. Zhou and his co-workers<sup>88</sup> guided by a top-down topological analysis, a MOF was constructed by pyrazolate-based (PZ-based) porphyrinic ligand, namely PCN-601, has been rationally designed and synthesized. The porphyrinic MOF with ftw-a topology is composed of the  $O_h$  symmetric 12-connected  $[Ni_8(OH)_4(H_2O)_2Pz_{12}]$  (which is denoted as  $[Ni_8]$ ) nodes and the  $D_{4h}$  symmetric 4-connected 5, 10, 15, 20-tetra(1H-pyrazol-4-yl)porphyrin ( $H_4TPP$ ) ligands (as **Fig. 3a**). Then, a series of tests have been carried out to identify the chemical stability of PCN-601. According to X-ray Diffraction (XRD) and BET

special surface area test, the crystallinity and porosity of PCN-601 can be greatly maintained between room temperature and 100 °C in saturated NaOH solution (20 mol L<sup>-1</sup>) (**Fig. 3b, c**). The experimental results suggest that designing porphyrin-based MOFs based on HSAB theory is crucial for the creation of acid and alkali resistant, as well as thermally stable, materials. This highlights the potential use of porphyrin-based MOFs in demanding catalytic environments in the future.

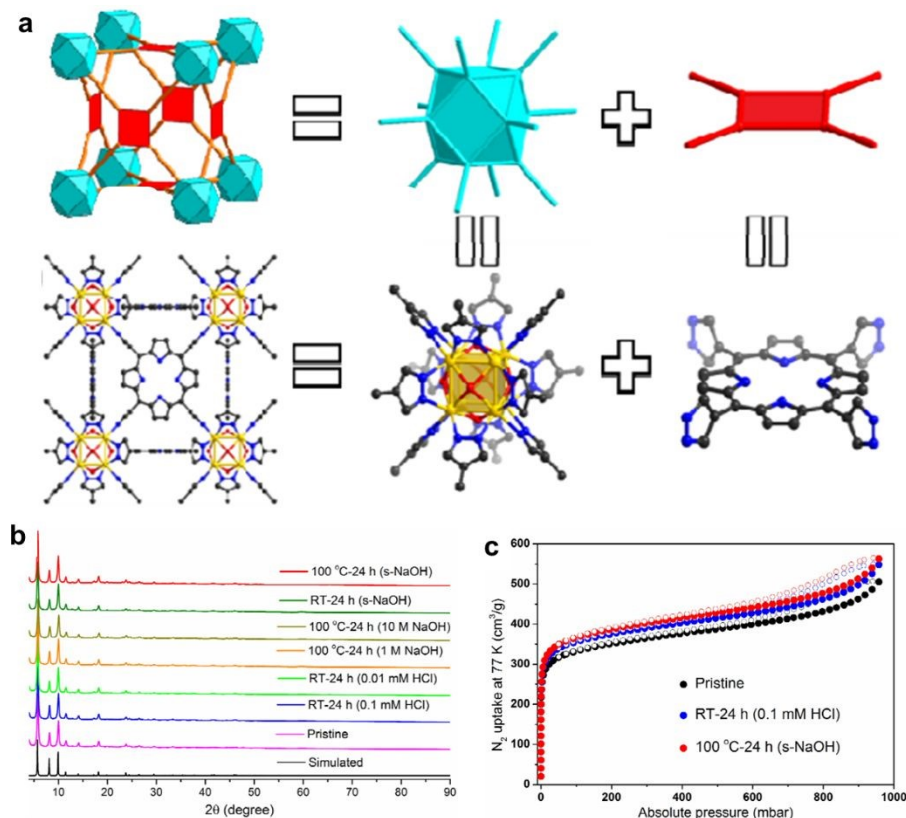


**Fig. 3.** (a) Structural analysis of PCN-601. (b) PXRD patterns for simulated, pristine PCN-601, and PCN-601 samples treated under different conditions. (c) N<sub>2</sub> adsorption/ desorption isotherms at 77 K of pristine PCN-601 and acid and base treated PCN-601 samples. Reproduced from ref. <sup>88</sup>. Copyright 2022 ACS.

Due to the distinctive structure of the porphyrin nucleus, the nitrogen atoms within the porphyrin cores of metalloporphyrin MOFs display a high reactivity towards coordination reactions with metal ions. By adjusting the metal ions within the ligands, changes in the photoelectronic properties of the porphyrin MOFs can be achieved. Therefore, controlling the coordination of metal ions proves to be a valuable method for improving the catalytic efficiency of metalloporphyrin MOFs. Gu and his team<sup>89</sup> reported a series of a series of 2D MOF Zn<sub>2</sub>[TCPP(M)] (named ZnTCPP(M), M = Zn, Mn, Fe, and H<sub>2</sub>) films engage in photodetectors and revealed the photodetection response of metalloporphyrin MOFs (**Fig. 4a, b**). In comparison to ZnTCPP(H<sub>2</sub>), ZnTCPP(Fe), ZnTCPP(Mn) and ZnTCPP(Zn), ZnTCPP(Zn) exhibited notable enhancement in photoresponse and light harvesting, which suggests great potential for research and applications in photoelectrocatalysis (as **Fig. 4c, d**). Furthermore, the topological guidance of the metalloporphyrin MOFs increases the number of ligand metal ions, promoting a uniform distribution of metal active sites. In

addition, integrating porphyrins containing different metal centers into porphyrin-based MOFs is expected to be a prominent research focus in the future. The metal-dependent photoelectrochemical properties are anticipated to play a key role in CO<sub>2</sub> catalytic reduction reactions.

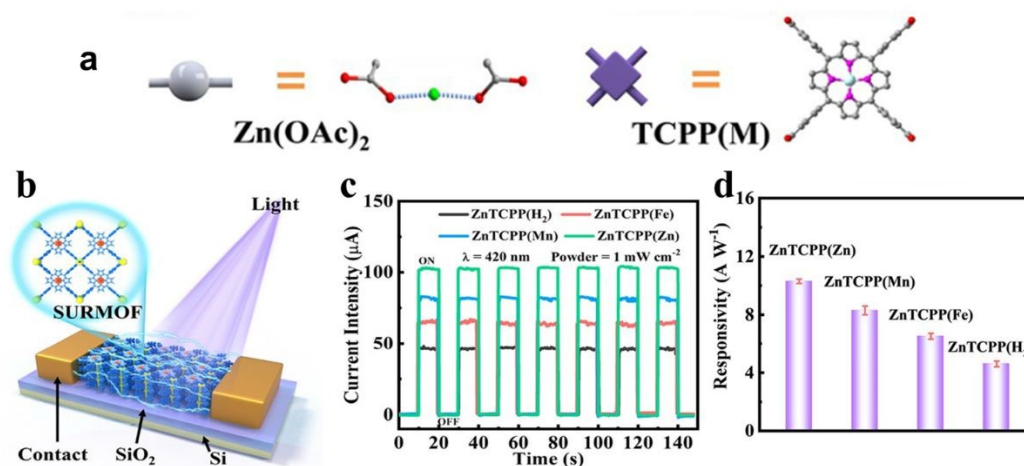


**Fig. 4.** (a) Preparation process of ZnTCPP(M) films. (b) Schematic diagram of ZnTCPP(M)-based photodetectors. (c) Photocurrent curve and (d) responsivities of the ZnTCPP(M)-based photodetector. Reproduced from ref. <sup>89</sup>. Copyright 2022 ACS.

### 2.1.2. Metal-organic cage engineering

Molecular organic cages are molecular structures composed of organic molecules that interact with each other to form a cavity structure. These cages are typically constructed by numerous organic molecules through non-covalent interactions, such as hydrogen bonding and hydrophobic effects, resulting in an organic molecular system with a hollow interior.<sup>53, 90, 91</sup> Hollow self-assembled molecular cages possess the remarkable capability to selectively include chemicals within their established cages. Additionally, they can aid in guest stabilization, storage, and transportation, as well as catalyze guest transformation in a controlled manner. Su *et al.* prepared two ultra-stable metal-organic frameworks ( $[Zr_6O_4(OH)_4(H_2TBPP)_3]_n \cdot (\text{solvent})_x$ ) (FJI-H6) and ( $[Hf_6O_4(OH)_4 \cdot (H_2TBPP)_3]_n \cdot (\text{solvent})_x$ ) (FJI-H7), which both feature 2.5 nm cages. FJI-H6 and FJI-H7 are both constructed from 12-connected  $M_6O_4(OH)_4(CO_2)_{12}$  nodes ( $M = Zr, Hf$ ) and porphyrin tetracarboxylic ligands ( $H_2TBPP = 4', 4''', 4''''', 4''''''-(\text{porphyrin-5, 10, 15, 20-tetrayl})\text{tetrakis}([1, 10\text{-biphenyl}]\text{-4-carboxylic acid})$ ) as **Fig. 5a-c**<sup>92</sup>. Gas adsorption experiments reveal the special surface area of FJI-H6 and FJI-H7 are 5007 m<sup>2</sup> g<sup>-1</sup> and 3831 m<sup>2</sup> g<sup>-1</sup>, respectively. FJI-H6 and FJI-H7 synthesized with metal-organic cage strategy exhibits a satisfied special surface area is much larger than that of PCN-222(Fe) (2200 m<sup>2</sup> g<sup>-1</sup>), NU-1000 (2320 m<sup>2</sup> g<sup>-1</sup>), PCN-223(Fe) (1600 m<sup>2</sup> g<sup>-1</sup>), PCN-94 (3377 m<sup>2</sup> g<sup>-1</sup>), NU-1100 (4020 m<sup>2</sup> g<sup>-1</sup>) and PCN-229 (4619 m<sup>2</sup> g<sup>-1</sup>), notably, among those Hf-based MOFs have been reported, FJI-H7 shows the best special surface area (**Fig. 5d**). Then, the acid and alkali resistance tests confirmed the stability of FJI-H6 and FJI-H7, as it exhibited excellent stability in aqueous solutions with pH value levels ranging from 0 to 10. However, it is worth

noting that the alkali resistance of this particularly organic cage-structured porphyrinic MOFs is slightly lower when compared to other structured MOFs. In addition, FJI-H6 and FJI-H7 have some catalytic effect on CO<sub>2</sub>, the catalytic mechanism is shown in **Fig. 5e**, which is mainly attributable to distribution of Lewis active sites on the porphyrinic MOFs.

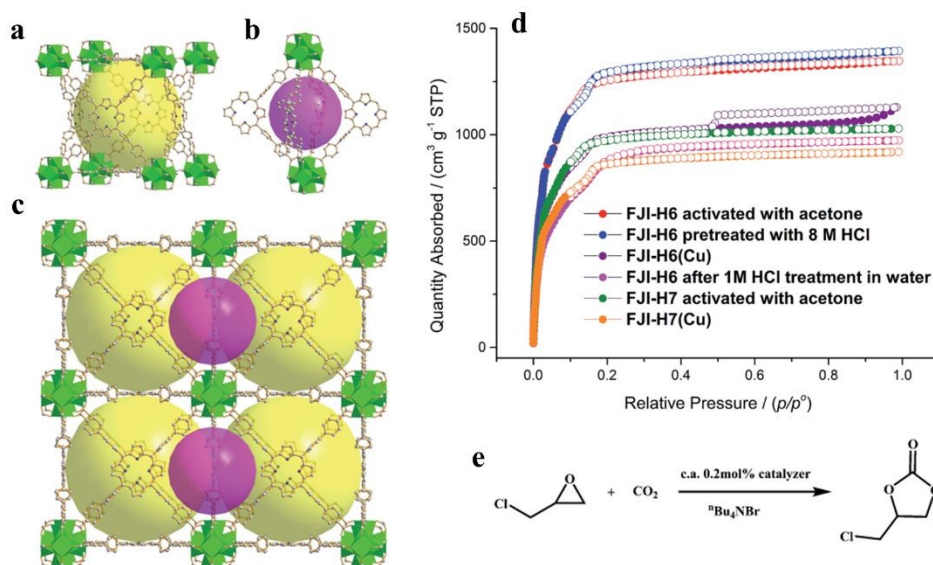


**Fig. 5.** (a) The large cubic cage constructed from six porphyrin ligands and eight Zr<sub>6</sub>O<sub>4</sub>(OH)<sub>4</sub> clusters. (b) The small octahedral cage constructed from four porphyrin ligands and two Zr<sub>6</sub>O<sub>4</sub>(OH)<sub>4</sub> clusters. (c) Packing of the two kinds of cages. (d) Experimental N<sub>2</sub> adsorption isotherms for FJI-H6, FJI-H6(Cu), FJI-H7 and FJI-H7(Cu). (e) Cycloaddition reactions of CO<sub>2</sub> with epoxide catalyzed by FJI-H6(Cu), FJI-H7 and FJI-H7(Cu). Reproduced from ref. <sup>92</sup>. Copyright 2022 RSC.

### 2.1.3. Pillar-layer engineering

Kitagawa and his collaborators were the first to propose the concept of pillars in MOFs<sup>90</sup>. In this structure, the layers are bonded to each other through hydrogen bonds, resulting in a 3D arrangement.<sup>93, 94</sup> The design and modification of 3D porous materials are the significant breakthrough owing to the widespread application of the materials for the guest molecule adsorption.<sup>95-97</sup> Pillar-layer engineering is a straightforward and efficient way to synthesize the 2D structure of porphyrinic MOFs into a 3D structure. Zhou *et al.* synthesized a mixed-linker zirconium-based metal-organic frameworks (Zr-MOFs) with a layer-pillar structure.<sup>98</sup> As **Fig. 6a, b**, 6-coordinated Zr<sub>6</sub> clusters with hexagonal shape and the triangular BTB linkers are interconnected to form a 2D layered (3, 6)-connected kdg topology. In addition, The Zr<sub>6</sub> metal clusters are not only bonded to the six carboxylate groups in the 2D layer, but they also have six pairs of terminal -OH/H<sub>2</sub>O ligands distributed on the upper and lower sides of the layer to allow the carboxylate linkers to attach. In simpler terms, the 2D layers are linked together using ditopic linkers like pillars, which allows the 2D layered MOFs to grow into a 3D layer-pillar structure. Noteworthy, the creation of Zr-carboxylic acid bonds is an exothermic process, making it energetically favorable

for MOFs with well-connected  $Zr_6$  clusters. The authors were thermodynamically guided to combine two rational linkers to convert the 6-connected  $Zr_6$  clusters to 12-connected one thereby realizing porphyrinic Zr-MOF with mixed linkers with the lowest system energy, namely  $Zr_6O_4[OH]_6[H_2O]_2[BTB]_2[TCPP]$  (PCN-134). The stability of the PCN-134 was demonstrated through using of XRD pattern and  $N_2$  sorption isotherms derived from single-crystal X-ray diffraction and BET experiments (Fig. 6c-d). The XRD patterns demonstrate that the structure of PCN-134 remains unchanged when it is exposed to aqueous solutions with pH values ranging from 0 to 13. However, there are slight variations in the intensity of the peaks observed in the XRD patterns. Combined with the results of  $N_2$  sorption isotherms, the acid-base tolerance test confirmed that the layered-pillars structure of PCN-134 remained stable without experiencing collapse or phase transition, indicating its high chemical stability. In addition to the high stability of mixed-linkers PCN-134, manipulating the proportions of various linkers, it is possible to enhance the adsorption capacity of mixed-linkers PCN-134 for guest molecules. As Fig. 6e, the TCPP ratio up to 25% in the PCN-134 framework the most performance of  $N_2$  uptake is exhibited ( $717 \text{ cm}^3 \text{ g}^{-1}$ ), which is mainly attributed to the defects between the Zr-BTB layers resulting from missing TCPP fragments. Furthermore, the 3D porphyrinic pillar-layered metal-organic framework promotes interlayer charge transfer more effectively. Fei Wang et al. synthesized porphyrinic pillar-layered MOF constructed with  $\pi$ -conjugated TCPP and *in-situ* formed 1, 2-bis-(1H- benzo[d]imidazol-2-yl)-ethene (BIE) conjugated ligands. In both PMOFs,  $Zn_2(CO_2)_4$  paddlewheel units are connected by TCPP-Zn ligands to form a 2D layer. The layers were connected by BIE ligands to form a porphyrinic pillar-layered MOF (PMOF-2). 3D pillar-layered PMOF-2 demonstrates strong light absorption within the visible light spectrum of 400-600 nm. Additionally, it displays impressive photoresponse in photocurrent experiments, primarily due to its exceptional conductivity.

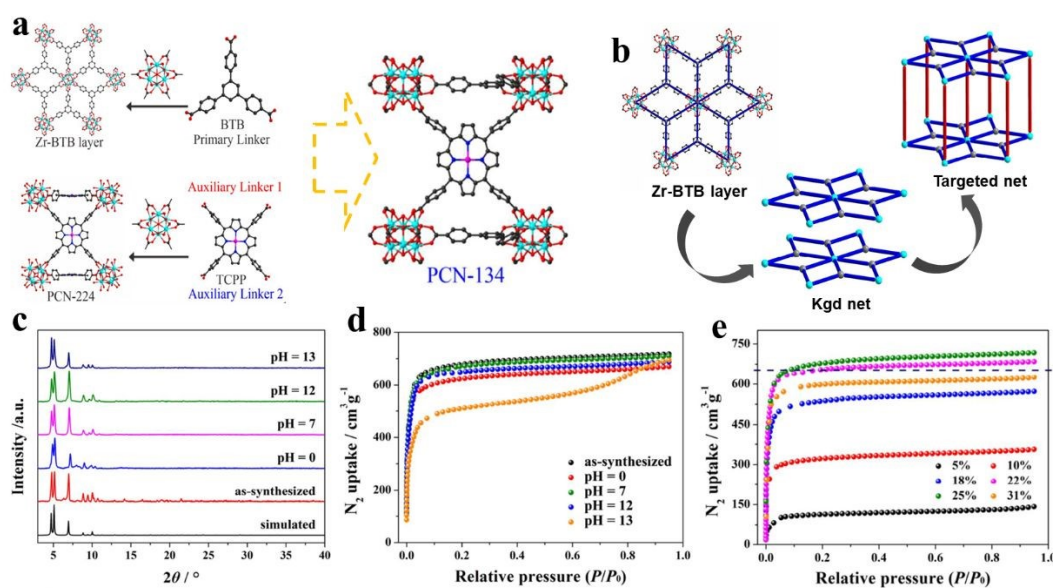


**Fig. 6.** Design of mixed-linker Zr-MOFs: (a-b) PCN-134 and PCN-224 formed by 6-connected  $Zr_6$  cluster and TCPP. (c) the XRD patterns and (d) the  $N_2$  isotherms after immersion in aqueous

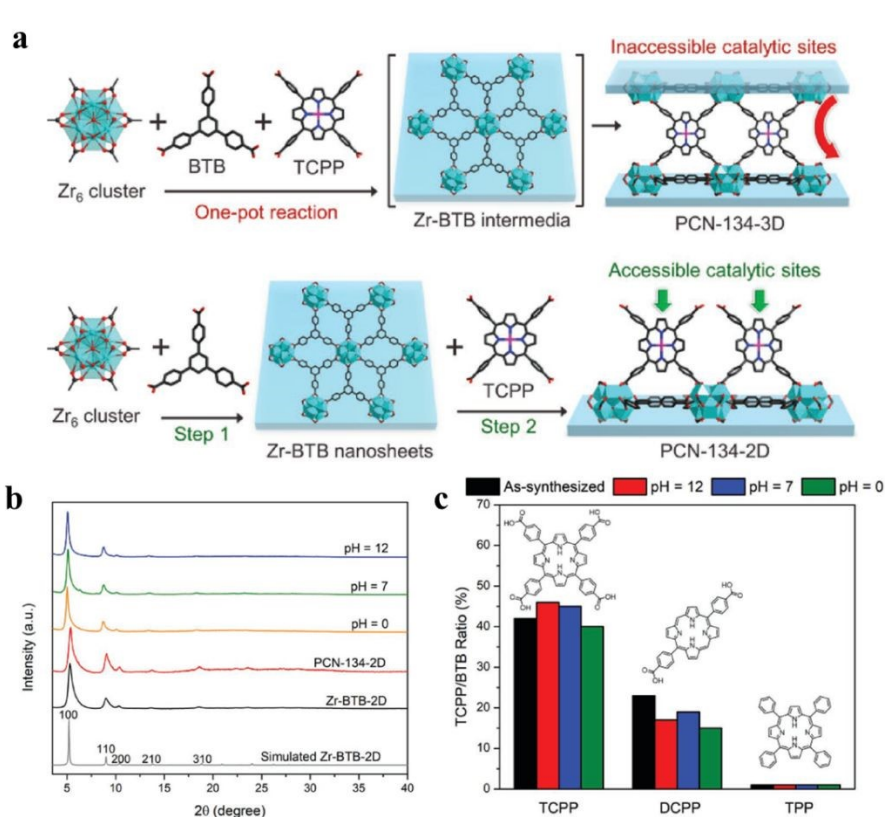
solutions with different pH values at room temperature for 24 h. (e) Effects of TCPP defects of PCN-134 system on N<sub>2</sub> uptake measured at 77 K. Reproduced from ref. <sup>98</sup>. Copyright 2022 ACS. View Article Online  
DOI: 10.1039/D4EE01748J

## 2.2. Porphyrin@MOFs

To create porphyrin@MOFs, we usually trap free-base porphyrins or metalloporphyrins inside the pores or attach them to the surface of MOFs, and employ *in-situ* formation or post-synthesis methods to integrate porphyrins into MOFs.<sup>47</sup> Because porphyrin molecules self-degrade and aggregate, porphyrin or metalloporphyrin-based catalysts are typically utilized in homogeneous catalytic systems, which significantly reduces their catalytic efficiency.<sup>55, 99</sup> The catalytic activity and stability of porphyrin can be enhanced by incorporating porphyrins into MOFs to create heterogeneous porphyrin@MOFs.

PCN-134 is a porphyrin-based MOFs consist of Zr-BTB and porphyrinic linkers with typical pillar-layer structure as the introduction of section 2.1.3. Zhou *et al.* successfully synthesized PCN-134-2D (functionalized MOF 2D nanosheet) and PCN-134-3D (functionalized MOF 3D nanosheet) through one-pot reaction and step-wise synthesis, and the processes were illustrated in **Fig. 7a**. Subsequent tests on the acid and alkali resistance of PNC-134-2D, modified with varied porphyrin groups, demonstrated that PNC-134-2D synthesized using step-wise method remained stable in the pH range of 1-10. PNC-134-2D produced through TCPP synthesis was found to be even more stable, likely due to its greater number of coordination groups. Abbreviations will be explained when first used. Yi and his group synthesized the stable metal organic framework PCN-224 through post-modification and embed Mn<sup>3+</sup> into the porphyrin@MOFs as prepared to form PCN-224(Mn). Moreover, compared with PCN-224 with special surface area of 2630 m<sup>2</sup> g<sup>-1</sup>, PCN-224(Mn) almost retains the specific surface area of PNC-24 while introducing a metal active center. The metalloporphyrin-based MOFs obtained through a post-synthesis method maintained structural stability during acid and alkali tests, with no detachment of metal ions observed.





View Article Online  
DOI: 10.1039/D4EE01748J

**Fig. 7.** (a) Schematic representation showing the one-pot synthesis of PCN-134-3D and stepwise synthesis of PCN-134-2D nanosheets with accessible catalytic sites. (b) PXRD of Zr-BTB and PCN-134-2D treated by aqueous solutions with different pH values. (c) Stability test of Zr-BTB modified by TCPP, DCPP, and TPP treated by aqueous solutions with different pH values. Reproduced from ref. <sup>100</sup>. Copyright 2022 Wiley.

Guided by topological engineering, metal-organic cage engineering, pillar-layer engineering and post-synthesis strategy, substantial porphyrin-based MOFs have been synthesized and modified by purpose, which means tremendous potential for research and application. Herein, high-value CO<sub>2</sub> conversion high demand exists for the distribution of catalyst active sites, specific surface area size, and stability. Metal-organic cage engineering can offer a significantly large specific surface area and uniformly distributed active sites for porphyrin-based MOFs. However, the metal nodes of metal-organic cage are generally classified as soft acids, which restricts the intensity of interactions between the ligand and center metals, thereby compromising stability. This issue has been subject to numerous criticisms. However, topological engineering broader selection of metals for metal nodes presents a noteworthy benefit in constructing porphyrin-based MOFs with stable structures. The issue of some functional groups being unable to be introduced directly during *in-situ* synthesis is resolved by introducing them to fine-tune the properties in the porphyrin-based MOFs or to functionalize the porphyrin-based MOFs on a larger scale. However, often the introduction of functional groups leads to a reduction in the specific surface area of porphyrin-based MOFs.

### 3. Basic principle for CO<sub>2</sub> reduction

The high symmetry and linear structure of CO<sub>2</sub> molecules result in evenly distributed electronic charges and spatial arrangement, leading to a low-energy state. Consequently, activating CO<sub>2</sub> necessitates the input of substantial energy. The photo(electro)catalytic CO<sub>2</sub> reduction using porphyrin-based MOFs is classified as a prototypical heterogeneous catalytic system, wherein CO<sub>2</sub> molecules undergo activation and subsequent evolution of intermediates at the porphyrin MOF surface.<sup>101</sup> Consequently, an in-depth investigation into the catalytic mechanisms and structure-activity relationships of porphyrin MOFs is of paramount importance.<sup>102</sup> Below is a detailed explanation of the CO<sub>2</sub> activation, the mechanisms involved and the structure-activity relationship in these systems.

#### 3.1. Surface interface catalysis mechanism

The processes of photocatalytic CO<sub>2</sub> reduction are generally divided into light absorption, electron injection, CO<sub>2</sub> activation and evolution of intermediates. Porphyrin rings possess 26- $\pi$  electrons, forming a highly conjugated electronic system. Conjugated systems enable  $\pi$  electrons to delocalize along the chain, creating a uniform electron cloud and molecular orbitals  $\pi$  and  $\pi^*$  with distinct energy levels. When the energy of photon matches the gap between these levels, absorption occurs. The continuous band-like energy structure of conjugated  $\pi$  electrons broadens their light absorption range, especially in the visible spectrum, allowing these compounds to capture diverse wavelengths.<sup>103</sup> Thus, porphyrin function as a vital constituent of porphyrin-based MOFs, endows porphyrin-based MOFs materials with exceptional absorption properties in the visible spectrum, enabling them to efficiently capture photons and instigate transitions to excited states. The electrons excited by photo energy are injected into the conduction band of the porphyrin-based MOFs, leaving positive holes ( $h^+$ ) in the porphyrin. The essence of this process lies in the transfer of photogenerated electrons to active sites on the porphyrin-based MOF, where they can engage in reduction reactions. Then, the injected electrons reduce adsorbed CO<sub>2</sub>, creating reactive intermediates (COOH\*, CO\*, OCHO\*) that are amenable to further reduction steps. Subsequently, the intermediates convert to target products, the sufficient reaction kinetics and the availability of photogenerated electrons are crucial factors for this process.<sup>104</sup>

Porphyrin-based MOFs functioning as electrocatalysts in the electrochemical CO<sub>2</sub> reduction of undergo a process akin to the general mechanism of CO<sub>2</sub> electroreduction, albeit with variations attributed to the specific properties of porphyrin moieties and metal centers.<sup>105</sup> The process initiates with the adsorption and activation of CO<sub>2</sub>.<sup>106</sup> Then, driven by an applied electric field or photoexcitation, electrons migrate from the electrode to the metal center and further to the CO<sub>2</sub> molecule.<sup>2</sup> Finally, a series of intermediates and target products are formed. Additionally, In the case of carefully designed porphyrin-based MOFs, their inherent

structural resilience and the capacity of their metal centers to undergo reversible redox transformations are pivotal to a phenomenon known as catalyst regeneration, which is essential for upholding catalytic activity after multiple operational cycles.<sup>107</sup> And porphyrin-based MOFs excel in photocatalytic applications primarily due to their conjugated structures and tunable pore architectures, which collectively enhance both conductivity and mass transfer efficiency.

View Article Online  
DOI: 10.1039/D4EE01748J

### 3.1.1 Adsorption and activation of CO<sub>2</sub>

The adsorption and activation of CO<sub>2</sub> on porphyrin-based MOFs are intricate processes that rely on the strategic design of the structure of porphyrin-based MOFs, composition, and functionality.<sup>108</sup> By optimizing these factors, researchers can enhance the interaction between CO<sub>2</sub> and the catalytic sites, thereby improving the efficiency and selectivity of CO<sub>2</sub> reduction reactions. Understanding and manipulating these mechanisms are critical steps towards developing Adv. mater. for sustainable energy conversion and carbon utilization technologies.

It is widely acknowledged that CO<sub>2</sub> adsorption is significantly influenced by factors such as the specific surface area, pore dimensions, and functional groups attached to porphyrins.<sup>109</sup> The synthesis of porphyrin-based MOFs predominantly involves strategies like topological engineering, layer-pillar schemes, and cage construction methodologies, thereby bestowing unique advantages in designing porphyrin MOFs with high surface areas and appropriately sized pores.<sup>110-112</sup> Furthermore, the tunability of porphyrin linkers implies enhanced regulatory capacity over CO<sub>2</sub> adsorption in porphyrin-based MOFs, offering improved modulation of their catalytic performance. Zhou and his team prepared PCN-601 composed of reactive Ni-oxo cluster nodes and light-harvesting metalloporphyrin ligands connected via pyrazolyl group, as a catalyst for gas-phase overall CO<sub>2</sub> photoreduction with H<sub>2</sub>O vapor at room temperature.<sup>113</sup> Comparison through BET analysis and CO<sub>2</sub> capture experiments has revealed that porphyrin-based MOFs generally possess substantial specific surface areas. While large surface areas have a notable impact on CO<sub>2</sub> adsorption, a critical factor in the kinetics of heterogeneous gas-solid reactions, particularly the affinities between reactants and the catalyst, was meticulously assessed in the case of PCN-601. Consequently, the substantial specific surface area provides an abundance of adsorption sites for CO<sub>2</sub>, and efficient adsorption is further augmented by the generation of photogenerated electrons under light irradiation. Additionally, this study confirmed that in PCN-601, these photogenerated electrons utilize Ni as a conduit, facilitating accelerated electron transfer and thereby enhancing the catalytic efficiency (**Fig. 8a**).

The activation of CO<sub>2</sub> is a pivotal step in its conversion into value-added chemicals and fuels. This process typically involves breaking the stable double bond between the carbon and oxygen atoms in CO<sub>2</sub>, rendering it reactive enough to participate in subsequent reduction reactions. Strategies to provide suitable reaction sites and lower the energy barrier for CO<sub>2</sub> activation in porphyrin-based MOFs primarily involve several methods: constructing metal ions coordinated within the

porphyrin ring, designing frameworks with synergistic multiple reactive sites, and engineering metal nodes to enhance conductivity. Xu demonstrated the CO<sub>2</sub> coordination can drive low temperature rapid synthesis of porphyrin-based bismuth-MOFs (Bi-PMOFs) by utilizing synergistic physical and chemical properties of supercritical CO<sub>2</sub>.<sup>114</sup> And SC-Bi-PMOFs combined many advantages of high accessible active sites, fast electron/mass transfer capability, and unique coordination environment around active sites, thus endowing them superior photocatalytic CO<sub>2</sub> reduction activity (**Fig. 8b**). In both photocatalytic and electrocatalytic CO<sub>2</sub> reduction, the provision of electrons with sufficient kinetic energy to the active sites is crucial for disrupting the inherent symmetry of CO<sub>2</sub> molecules, thereby facilitating the activation of CO<sub>2</sub>. This step is pivotal in converting CO<sub>2</sub> into value-added chemicals or fuels.

### 3.1.2 Evolution of intermediates

As stated above, photocatalysis of porphyrin-based MOFs harnesses light to generate excited electrons that engage in surface reactions with CO<sub>2</sub>, whereas electrocatalysis relies on electric fields to drive the process.<sup>115</sup> Consequently, the efficacy of photocatalytic reactions with porphyrin-based MOFs is largely dependent on their bandgap structures that dictate light absorption and electron-hole pair generation. Conversely, in the context of electrocatalysis, emphasis shifts towards optimizing mass transfer efficiency and ensuring a favorable distribution of charges at the active sites for efficient electron transfer. However, the evolution process of CO<sub>2</sub> and intermediates during both photocatalysis and electrocatalysis is strikingly similar, as follow:

One step:  $*\text{COOH} + e^- \rightarrow \text{CO} + \text{OH}^-$

Two steps:  $*\text{COOH} + e^- \rightarrow * \text{CO} + \text{OH}^- \rightarrow \text{CO} + \text{H}_2\text{O}$

$* \text{CO} + e^- + \text{H}^+ \rightarrow * \text{CHOH} \rightarrow \text{CH}_3\text{OH}$

Multi-step:  $* \text{CO} + 2e^- + 2\text{H}^+ \rightarrow * \text{CHOHCH}_2 \rightarrow \text{C}_2\text{H}_4$

$* \text{CO} + 2e^- + 2\text{H}^+ \rightarrow * \text{CHOHCH}_2\text{OH} \rightarrow \text{CH}_3\text{CH}_2\text{OH}$

Recently, surface interface catalysis mechanism of photo(electro)catalytic CO<sub>2</sub> reduction for porphyrin-based MOFs shows different ideals due to the complex structure of porphyrin-based MOFs. Generally, redox-active sites of porphyrin-based MOFs are typically situated at the metal centers within their structure, where these centers possess a unique electronic configuration enabling participation in redox reactions and facilitation of electron transfer. Zhang and his team prepared porphyrin-based MOFs (Cu-SAs@Ir-PCN-222-PA) with dual active sites of Ir-porphyrin and Cu-SAs through the pre-coordination confinement strategy. Catalytic results disclosed that Cu-SAs@Ir-PCN-222-PA could drive the reduction of CO<sub>2</sub> to C<sub>2</sub>H<sub>4</sub> with a high faradaic efficiency (FE) (70.9%) with the current density of 20.4 mA cm<sup>-2</sup>. And the DFT Calculation was carried to deduce the electrocatalytic CO<sub>2</sub> reduction mechanism ( $2\text{CO}_2 + 8e^- + 8\text{H}^+ \rightarrow \text{C}_2\text{H}_4 + 2\text{H}_2\text{O}$ ). The reduction of CO<sub>2</sub> molecules at the catalyst surface involves a sequential acquisition of electrons and protons, namely, a stepwise electron transfer proton transfer (ET-PT).

Distinguished traditional redox mechanism, in proton-coupled electron transfer (PCET), the transfer of electrons is tightly coupled with that of protons, occurring virtually simultaneously, which contrasts with traditional redox reactions where electron and proton transfers may occur as separate steps.<sup>114</sup> Moreover, the thermodynamic and kinetic properties of PCET reactions can vastly differ from those of isolated electron or proton transfers. This synergistic transfer can impact the free energy change, activation energy, and reaction rate, sometimes rendering reactions feasible that would otherwise be difficult to proceed. Sarazen and co-workers well-dispersed iron-porphyrin-based MOF (PCN-222(Fe)) on carbon-based electrodes revealed optimal turnover frequencies for CO<sub>2</sub> electroreduction to CO at 1 wt.% catalyst loading, beyond which the intrinsic catalyst activity declined due to CO<sub>2</sub> mass transport limitations.<sup>116</sup> The pattern of  $\log(j_{\text{CO}})$  vs.  $\log(\text{HCO}_3^-)$  indicates that the CO<sub>2</sub> electroreduction rate is not dependent on the transfer of protons. This finding excludes both PT in the stepwise ET-PT pathway and PCET as the rate-determining step of the reaction, suggesting that ET is the rate-determining step (**Fig. 8c**).

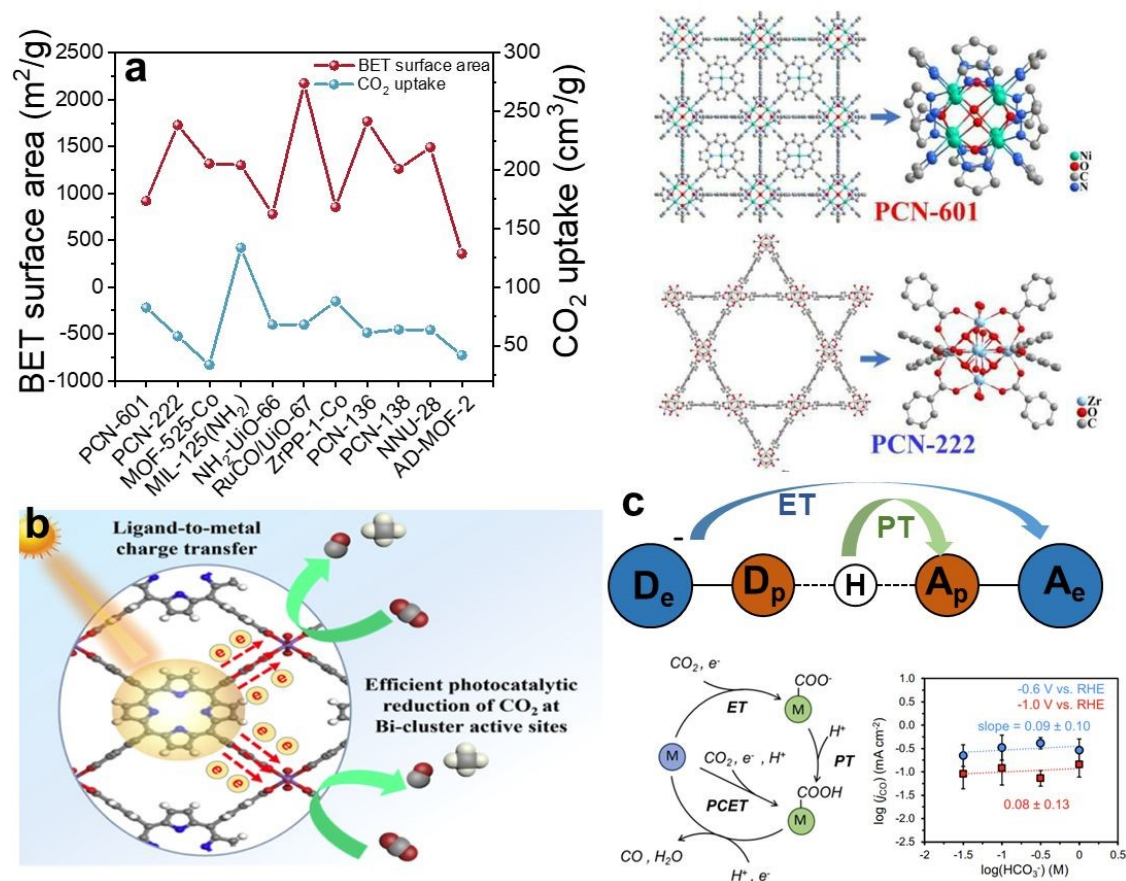


**Fig. 8.** (a) The BET surface area and the CO<sub>2</sub> uptake of PCN-601 and the structure of PCN-601 and PCN-222. Reproduced from ref.<sup>113</sup>. Copyright 2022 ACS. (b) the electron-transfer mechanisms of SC-Bi-PMOFs. Reproduced from ref.<sup>114</sup>. Copyright 2022 ELSEVIER. (c) The mechanisms of ET-PT and PCET and the pattern of  $\log(j_{\text{CO}})$  vs.  $\log(\text{HCO}_3^-)$ . Reproduced from ref.<sup>116</sup>. Copyright 2022 WILEY.

### 3.2 Structure-activity relationship

Porphyrin-based MOFs have emerged as prominent catalysts in the realm of Adv. mater., primarily due to their integration of unique structural elements: a porphyrin core offering tunable electronic properties, strategically selected metal nodes that facilitate electron transfer, meticulously designed linkers enabling porosity tuning, and a highly ordered porous structure providing enhanced surface areas. This sophisticated design not only fosters exceptional photo(electro)catalytic functionality for efficient CO<sub>2</sub> conversion into valuable chemicals and fuels but also underscores their stability and recyclability, which are pivotal for sustainable carbon capture and utilization technologies. The synergy of these features positions porphyrin-based MOFs as prime candidates in the quest for optimized photocatalytic and electrocatalytic systems, thereby driving advancements in green chemistry and climate change mitigation strategies.

The porphyrin core serves as a common reactive site in porphyrin-based MOFs for photo(electro)catalytic CO<sub>2</sub> reduction, primarily due to its facile coordination capabilities and ability to easily accept and transfer electrons. When the macrocyclic porphyrin structure coordinates with metal ions, it effectively captures light energy and facilitates electron excitation and transfer, which is vital for activating CO<sub>2</sub> molecules. With metal ions situated at the center of the porphyrin ring, they can modulate charge distribution, influencing the electronic structure of the catalytic site and, consequently, altering the adsorption and activation abilities towards reactants such as CO<sub>2</sub>. Furthermore, tuning the metal species within the porphyrin core allows for further optimization of catalytic performance, as different metal centers impart distinct electronic characteristics and activities, advantageous in breaking the symmetry of CO<sub>2</sub> and promoting its conversion into valuable chemicals and fuels during photocatalysis or electrocatalysis.<sup>29, 117</sup> Su and his team contrastively investigate the catalytic performance of the two-dimensional (2D) cobaltporphyrin-based organic frameworks linked with phenyl, CoO-cluster, ZnO-cluster, and ZrO-cluster, as CO<sub>2</sub> reduction photocatalysts (abbreviated as CoP, Co-PMOF, ZnPMOF, and Zr-PMOF, respectively) using DFT computations. The calculated results represent that the CoP, Co-PMOF, Zn-PMOF, and Zr-PMOF monolayers are all semiconductors with band gaps of 1.63, 1.21, 1.72, and 1.68 eV, respectively.<sup>118</sup> A narrower bandgap implies superior light-harvesting capability, hence modifications to the porphyrin core are conducive to enhancing the electronic environment around the porphyrin, thereby elevating the catalytic performance of porphyrin-based MOFs. The selection of metal nodes in porphyrin-based MOFs not only directly influences the electronic structure of the MOFs but also interacts synergistically with the porphyrin units, collectively enhancing the catalytic performance of porphyrin-based MOFs. Sheng fabricated a Cu-ZnTCPP MOF, in which the first Cu refers to the carboxylate-coordinated Cu<sub>2</sub>(COO)<sub>4</sub> node in a paddle-wheel structure.<sup>119</sup> The research exhibited that the enhanced CO<sub>2</sub> reduction rate in the presence of O<sub>2</sub> benefited from the promoted activity on the higher coordination Cu node (HO-Cu node) relative to that on the lower coordination Cu node (LC-Cu node) with a significantly lower activation

barrier (0.55 eV vs. 1.42 eV), as well as the role of -OH in capturing and activating the gas-phase CO<sub>2</sub>. The judicious introduction of functional groups markedly enhances the photocatalytic performance of porphyrin-based MOFs by widening the light absorption range, refining charge transport efficiency, creating and tuning active sites, and fostering synergies. Additionally, it bolsters their electrocatalytic capabilities through improvements in conductivity and modulation of local charge distribution, thereby comprehensively elevating both photo(electro)catalytic efficiencies. Chen synthesized a series of functional group-containing (-F, -NH<sub>2</sub> and -NO<sub>3</sub>) MOF-808 catalysts and investigated their adsorption behavior toward CO<sub>2</sub>. F-MOF-808 exhibited super catalytic performance for CO<sub>2</sub>, which underscore the significance of rationally tuning the electronic structure and defective metal centers. Furthermore, the introduction of fluorine significantly enhanced the selectivity towards CO production for F-MOF-808, reaching up to 97.8%.<sup>120</sup>

Porphyrin-based MOFs have demonstrated remarkable potential in the fields of photo(electro)catalysis for CO<sub>2</sub> reduction, with the exploration of their high-performance characteristics primarily centered around three core aspects: CO<sub>2</sub> adsorption and activation, evolution of intermediates, and the relationship between structure and activity. Firstly, the adsorption and activation of CO<sub>2</sub> mark the inception of the entire catalytic process.<sup>121-123</sup> The unique porous architecture of porphyrin-based MOFs, coupled with functionalized ligands, enhances both the physical adsorption and chemical activation of CO<sub>2</sub> molecules. Particularly, tuning the functional groups on the porphyrin ring can optimize the binding mode of CO<sub>2</sub> at active sites, reducing its activation energy barrier and facilitating the initial step of CO<sub>2</sub> conversion. Secondly, the evolution of intermediates is pivotal to gaining an in-depth understanding of the catalytic mechanism. Under photo or electrostimulation, the formation, stabilization, and transformation pathways of intermediates generated post-CO<sub>2</sub> activation, such as \*COOH and \*CHO, directly influence the selectivity and yield of the final products. Furthermore, the proposition of PCET mechanisms offers profound insights into the intricate interplay of electron and proton migration in photo(electro)catalytic CO<sub>2</sub> reduction, facilitating a deeper understanding of the reaction pathways involved. Lastly, the investigation of structure-activity relationships elucidates the microcosmic principles underlying catalyst design. Variations in metal nodes, linking strategies, and degrees of functionalization not only impact the electronic structure and photo(electro)responsive properties of the materials but also directly relate to the distribution and efficiency of catalytically active sites. Systematically adjusting these structural parameters uncovers new avenues for enhancing catalytic performance. In summary, by focusing on CO<sub>2</sub> adsorption and activation, tracing the progression of intermediates, and delving into the intrinsic connections between structure and activity, research on porphyrin-based MOFs for photocatalytic and electrocatalytic CO<sub>2</sub> reduction is progressively advancing our comprehension of efficient CO<sub>2</sub> conversion mechanisms. This endeavor provides a scientific foundation and innovative perspectives for the development of sustainable carbon cycle utilization technologies.

View Article Online  
DOI: 10.1039/D4EE01748J

#### 4. Porphyrin-based MOFs for photocatalytic CO<sub>2</sub> reduction

Photocatalyst plays an important role in the field of photocatalytic CO<sub>2</sub> reduction because of the process of transform CO<sub>2</sub> into add-value chemical (such as, CO, CH<sub>4</sub>, HCHO, HCOOH, CH<sub>3</sub>OH and C<sub>2</sub> products) through sunlight is straightforward and zero consumption. The materials that can be used as photocatalysts include semiconductors (ZnO<sub>2</sub>, TiO<sub>2</sub>, Fe<sub>2</sub>O<sub>3</sub>, CdS, Co<sub>3</sub>S<sub>4</sub> and LDHs etc.),<sup>9, 124</sup> semiconductors (porphyrin, triazine etc.), and noble metals (Ag nanoparticle (NPs), Au NPs, Pt NPs).<sup>28, 30</sup> When sunlight irradiate on the surface of photocatalyst, the process of photocatalytic reaction occurs on the surface as follow: 1) CO<sub>2</sub> molecules are absorbed by active sites of photocatalyst; 2) light harvesting of semiconductor photocatalyst; 3) Light energy drives the separation of photogenerated carriers; 4) The photogenerated carriers migrate to the semiconductor's valence (VB) and conduction (CB) bands, respectively; 5) The photogenerated electrons in the CB undergo a reduction reaction with the adsorbed CO<sub>2</sub>; 6) Products desorption from photocatalyst surface. This completes the entire catalytic reaction process. In contrast, the photocatalytic activity of noble metal NPs is rooted in the surface plasmon resonance effect (SPR).<sup>123, 125, 126</sup> The evidence presented demonstrates that the condition of photogenerated carriers significantly impacts the performance of photocatalysis.<sup>45, 112</sup> Porphyrins are highly efficient photo-response molecules, and functionalized porphyrins integrated into MOFs greatly improve the intra-electronic environment of the catalysts, thereby leading to intensive investigations. Porphyrin-based MOF(Zn) materials have strong photocatalytic activity for photocatalytic CO<sub>2</sub> reduction. S. Sharifnia and his co-workers synthesized porphyrin-based metal organic framework (Zn/PMOF), the ligand in Zn/PMOF is TCPP (**Fig. 9a**).<sup>127</sup> Then, Photocatalytic CO<sub>2</sub> reduction behavior of porphyrin-based MOFs was investigated by a platform of Zn/PMOF with a gaseous phase reactor, in which vapor act as donor. As shown in **Fig. 9b**, under UV/Visible irradiation, electrons at first are excited from the highest occupied molecular orbital (HOMO) to the lowest unoccupied molecular orbital (LUMO) of Zn/PMOF. Subsequently, the interaction between the photogenerated electrons in the CB and the adsorbed CO<sub>2</sub>, as well as the interaction between the photogenerated holes in the VB and the water molecules, initiates the photocatalytic reaction. In this photocatalytic system, the ultimate product is CH<sub>4</sub> with a considerable yield of 8.7 μmol g<sup>-1</sup> h<sup>-1</sup>. In addition, the results of 3-cycling and long-term tests illustrated that the porphyrin-based MOFs possessed excellent stability during the photocatalytic reaction (**Fig 9c, d**).



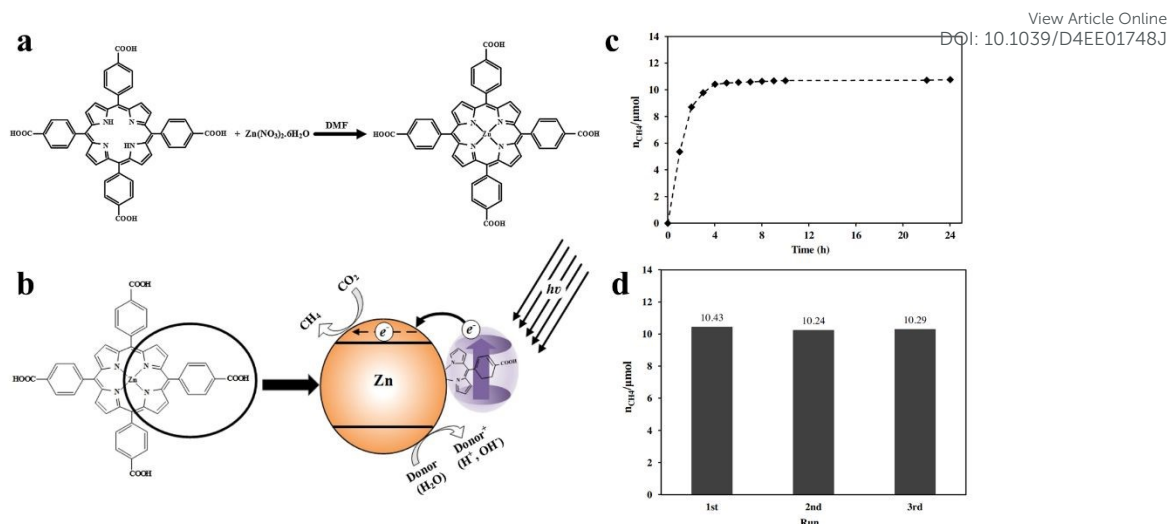


**Fig. 9.** (a) Synthetic reaction scheme for Zn/PMOF. (b) Mechanism of photocatalytic reduction of CO<sub>2</sub> over Zn/PMOF with H<sub>2</sub>O vapor as sacrificial agent. (c) The photocatalytic performance of Zn/PMOF under UV/Visible light after. (d) Recycling tests for photocatalytic reduction of CO<sub>2</sub> under UV/Visible light over Zn/PMOF. Reproduced from ref. <sup>127</sup>. Copyright 2022 ELSEVIER.

The chemical stability and the selection of active center of photocatalyst is a key factor for photocatalytic CO<sub>2</sub> reduction. diverse and complex structures of porphyrin-based MOFs demonstrate reliable stability of photocatalyst closely associated to the suitable synthesis routes and structural designs. Li and his team proposed a strategy that a series of BUT-110 with different contents of 4, 4'-(porphyrin-5, 15-diyl)dibenzolate (DCPP<sup>2-</sup>) were prepared by *in-situ* substitution of porphyrin ligands DCPP<sup>2-</sup> to stabilize and functionalize BUT-109(Zr).<sup>128</sup> And the post-synthetic route for DCPP<sup>2-</sup>-displaced BUT-109(Zr) (BUT-109(Zr)-P) also be carried. Then, the post-synthetic modification would not be applicable for BUT-109(Zr)-P owing to its low porosity resulted from framework interpenetration (**Fig. 10a**). According to the results of XRD and BET, BUT-109(Zr), BUT-110 analogs represent more chemical stability, which can be reflect on the PH tolerance (PH = 1-10) (**Fig. 10b, c**). As a comparison, BUT-109(Zr) possesses a poor chemical stability that mainly attributes to the reversible C-N linkage in the imide ligand inker 4, 4'-(1, 3, 6, 8-tetraoxobenz[*lmn*][3, 8]phenanthroline-2, 7(1H, 3H, 6H, 8H)-diyl)dibenzoate (NDIDB<sup>2-</sup>). In addition, metalloporphyrin act as excellent active site was induced into the most stability BUT-109(Zr)-50% through pre-synthesis to obtain a novel BUT-110-50%-Fe, which was applied in the study of photocatalytic CO<sub>2</sub> reduction. And the test about photocatalytic CO<sub>2</sub> reduction were performed in a reaction chamber charged with CO<sub>2</sub> (0.1 MPa) under full-spectrum irradiation, the hydrogen donor and the sacrificial agent are H<sub>2</sub>O and triethylamine, respectively. As **Fig. 10d**, the yield of main product (CO) for BUT-110-50%-Fe achieved 47.2 μmol g<sup>-1</sup> h<sup>-1</sup>, which could be demonstrated the robust porous structure and uniform active sites distribution synergistically promote photocatalytic CO<sub>2</sub> reduction performance.

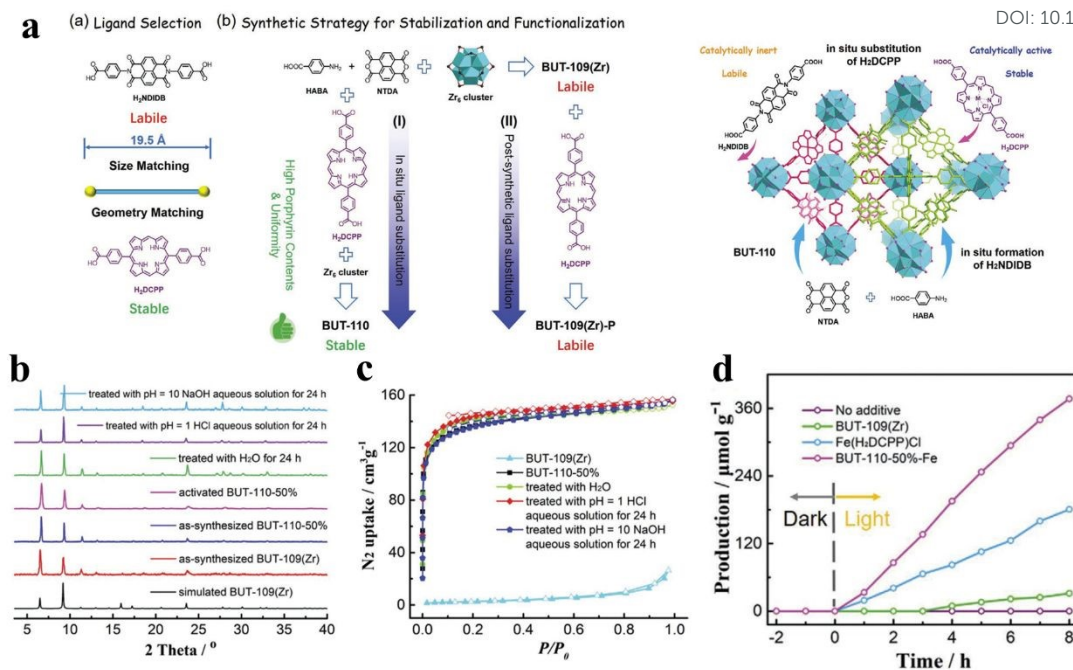
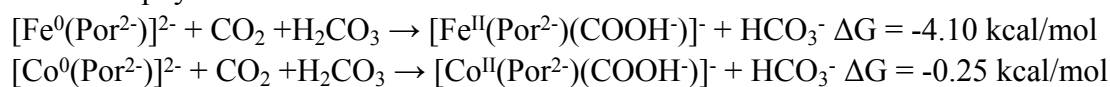


**Fig. 10.** (a) Ligand selection and synthetic strategies of BUT-110 through *in-situ* ligand substitution and post-synthetic ligand substitution, and the schematic illustration of the proposed “in-situ ligand substitution” strategy for the construction of BUT-110 from HABA, NTDA, and H<sub>2</sub>DCPP. (b) comparison of XRD patterns. (c) N<sub>2</sub> adsorption isotherms between BUT-109(Zr) and BUT-110-50% after different treatments. (d) The yield of CO for BUT-110-50%-Fe. Reproduced from ref. <sup>128</sup>. Copyright 2022 WILEY.

Porphyrins are integrated into MOFs as the functional moiety, altering the ligand metal positioned at porphyrin core towards the modulation of CO<sub>2</sub> photocatalysis is accessible. Wang and his team synthesized a series of 2-fold interpenetrated indium-porphyrin framework In(H<sub>2</sub>TCPP)<sub>(1-n)</sub>[M(TCPP)(H<sub>2</sub>O)]<sub>(1-n)</sub>[DEA]<sub>(1-n)</sub> (In-M<sub>n</sub>TCPP-MOF) (M = In, Co, Fe), which is consist of H<sub>2</sub>TCPP = tetrakis(4-benzoic acid)porphyrine with Fe coordination and DEA = diethylamine) (**Fig. 11a**)<sup>129</sup>. The photocatalytic CO<sub>2</sub> reduction test was performed in the mixed solution of 20 mg of L-ascorbic acid palmitate (L-AP) and 5 mL of ethyl acetate. Herein, high-performance visible-light-driven CO<sub>2</sub> to CO conversion is resulted by the synergetic effect between porphyrinic rings and Fe reaction active sites, and the performance of photocatalytic CO<sub>2</sub> reduction for the best catalyst (Fe<sub>1.91</sub>TCPP-MOF) up to 3469 μmol g<sup>-1</sup> within 24 h with high selection of 90% (**Fig. 11d**). According to the results of density functional theory (DFT) (**Fig. 11b**), COOH<sup>-</sup> is an important intermediate in the process of photocatalytic CO<sub>2</sub> reduction. Free energy changes for the CO<sub>2</sub> reduction processes at Fe/Co Porphyrins as follow:



The [Fe<sup>II</sup>(Por<sup>2-</sup>)(COOH<sup>-</sup>)]<sup>-</sup> origin from [Fe<sup>0</sup>(Por<sup>2-</sup>)]<sup>2-</sup> with a lower free energy than that [Co<sup>II</sup>(Por<sup>2-</sup>)(COOH<sup>-</sup>)]<sup>-</sup> transform from [Co<sup>0</sup>(Por<sup>2-</sup>)]<sup>2-</sup>, which means more stability for [Fe<sup>II</sup>(Por<sup>2-</sup>)(COOH<sup>-</sup>)]<sup>-</sup> compare with [Co<sup>II</sup>(Por<sup>2-</sup>)(COOH<sup>-</sup>)]<sup>-</sup>. The phenomenon is attributed to the self-filled d<sub>z<sup>2</sup></sub> orbital weakens the coordination of the

COOH<sup>-</sup> moiety from the z-direction for [Co<sup>0</sup>(Por<sup>2-</sup>)]<sup>2-</sup>. However, the empty d<sub>z<sup>2</sup></sub> orbital of [Fe<sup>0</sup>(Por<sup>2-</sup>)]<sup>2-</sup> can easily accept the long pairs of electrons from COOH<sup>-</sup>. Thus, Fe center is accessible to lower the negative charge of COOH<sup>-</sup> moiety, ultimately, stabilizing intermediate. Then, the short life-span of Fe<sub>1.91</sub>TCPP-MOF means the rapid recombination or the fast transportation of photogenerated carriers (Fig. 11c). The electrons property and CO<sub>2</sub> adsorption of Fe<sub>1.91</sub>TCPP-MOF demonstrate the rapid electrons migration may occurs on the photocatalyst. In addition, compared with [Co<sup>II</sup>(Por<sup>2-</sup>)(COOH<sup>-</sup>)]<sup>-</sup>, Fe active site brings key intermediates closer together (1.9 Å), which means the adsorption state has a low Gibbs free energy.

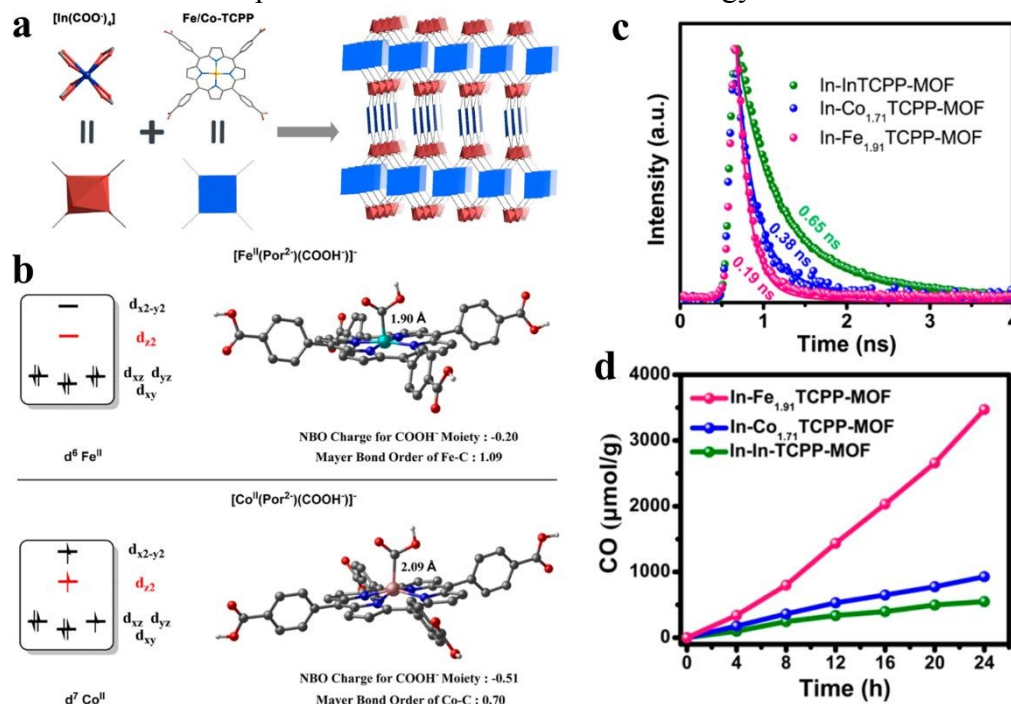


**Fig. 11.** (a) Synthesis and structure of the In-Fe/CoTCPP-MOFs. (b) Influence of the electron configurations of the metal centers on the metal-carbon interactions in [Fe<sup>II</sup>(Por<sup>2-</sup>)(COOH<sup>-</sup>)]<sup>-</sup> and [Co<sup>II</sup>(Por<sup>2-</sup>)(COOH<sup>-</sup>)]<sup>-</sup>. (c) Time-resolved PL decays of In-Fe<sub>1.91</sub>TCPP-MOF, In-Co<sub>1.71</sub>TCPP-MOF, and In-InTCPP-MOF under excitation at 440 nm. (d) Time profiles for the CO evolution catalyzed by In-Fe<sub>1.91</sub>TCPP-MOF, In-Co<sub>1.71</sub>TCPP-MOF, and In-InTCPP-MOF under irradiation with a 300 W xenon light (>400 nm) in the presence of 0.1 M L-ascorbic acid palmitate (L-AP) in ethyl acetate under 1 atm CO<sub>2</sub>. Reproduced from ref. <sup>129</sup>. Copyright 2022 ACS.

The life-span of photogenerated carrier is a significant influence for photocatalytic CO<sub>2</sub> reduction, which can be regulated through modifying the microstructure and permanent channels of porphyrin-based MOFs. Deria and his co-workers report topological control over the photophysical properties of MOFs via modular interchromophoric electronic coupling to manifest different their corresponding fluorescence lifetimes.<sup>130</sup> There are four samples target for lifetime research, NU-902(H<sub>2</sub>) and MOF-525(H<sub>2</sub>) are consisting of free-base TCPP(H<sub>2</sub>), and NU-902(Zn) and MOF-525(Zn) are consisting of zinc(II)-metallated TCPP(Zn) linkers. In addition, NU-902 with topological network of ftw and MOF-525 with topological network of scu manifest the smallest porphyrin-porphyrin torsional angle of 90° and 60°, respectively (Fig. 12a-c). According to Fig. 12d, e, the order of

fluorescence lifetime for the corresponding Zn(II)-based porphyrinic MOFs is  $\text{TCPPOMe(Zn)} > \text{MOF-525(Zn)} > \text{NU-902(Zn)}$  and the same trend appears on  $\text{TCPPOMe(H2)} > \text{MOF-525(H2)} > \text{NU-902(H2)}$ . Combined topological structures (ftw and scu) of porphyrin-based MOFs and fluorescence lifetime spectra indicate that stronger interchromophoric interaction occurs on the NU-902 and leads to more red shifted spectra with faster emissive state radiative decay. Therefore, the idea is potential to be applied in the investigation of photocatalytic  $\text{CO}_2$  reduction.

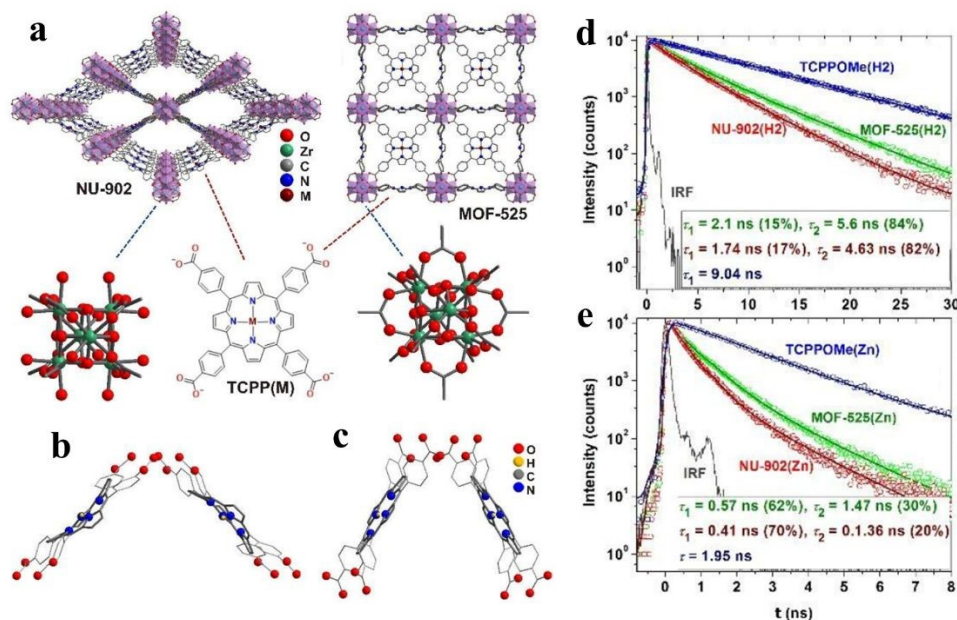


**Fig. 12.** (a) Molecular structures of porphyrin-based MOFs NU-902 and MOF-525 (M = H2 or Zn) and their corresponding building blocks. (b-c) DFT optimized structures of closely positioned porphyrin dimers in MOF-525(H2) [ $90^\circ$ ,  $d_{\text{M-M}} = 13.5 \text{ \AA}$ ] and NU-902(H2) [ $60^\circ$ ,  $d_{\text{M-M}} = 10.5 \text{ \AA}$ ]. (d-e) Transient emission decay profile for free-base and zinc(II)-metallated NU-902 and MOF-525. Reproduced from ref. <sup>130</sup>. Copyright 2022 RSC.

Single-atom strategy has been widespread employed in the field of photocatalytic  $\text{CO}_2$  reduction. The addition of single atoms enables a better dispersion of the reactive sites, while optimizing the photoelectronic properties of photocatalyst. Ye *et al.* incorporated coordinatively unsaturated Co single atoms into a porphyrin-based MOFs, notes as MOF-525-Co that is consist of  $\text{Zr}_6$  clusters and porphyrin-based molecular units (TCPP) as **Fig. 13a**.<sup>131</sup> In this photocatalytic system, single-atom Co is identified as the active site, as shown in **Fig. 13b**. This active site enhances the absorption of  $\text{CO}_2$  by increasing the concentration of localized electrons in the near-surface region and inducing surface corrugation. The introduction of electrons to the Co active sites lowers the reaction activation energy of  $\text{CO}_2$  (reducing the energy barrier (EB) from 4.13 to 3.08 eV), suggesting that photo-excited electrons from porphyrin migrate to  $\text{CO}_2$  molecules through the Co active site (**Fig. 13c, d**). Ultimately, the performance of optimal photocatalyst up to 3.13-fold improvement in CO evolution rate ( $200.6 \mu\text{mol g}^{-1} \text{h}^{-1}$ ) and a 5.93-fold enhancement in  $\text{CH}_4$  generation rate ( $36.67 \mu\text{mol g}^{-1} \text{h}^{-1}$ ) compared to the primitive porphyrin-based MOF (**Fig. 12e**).

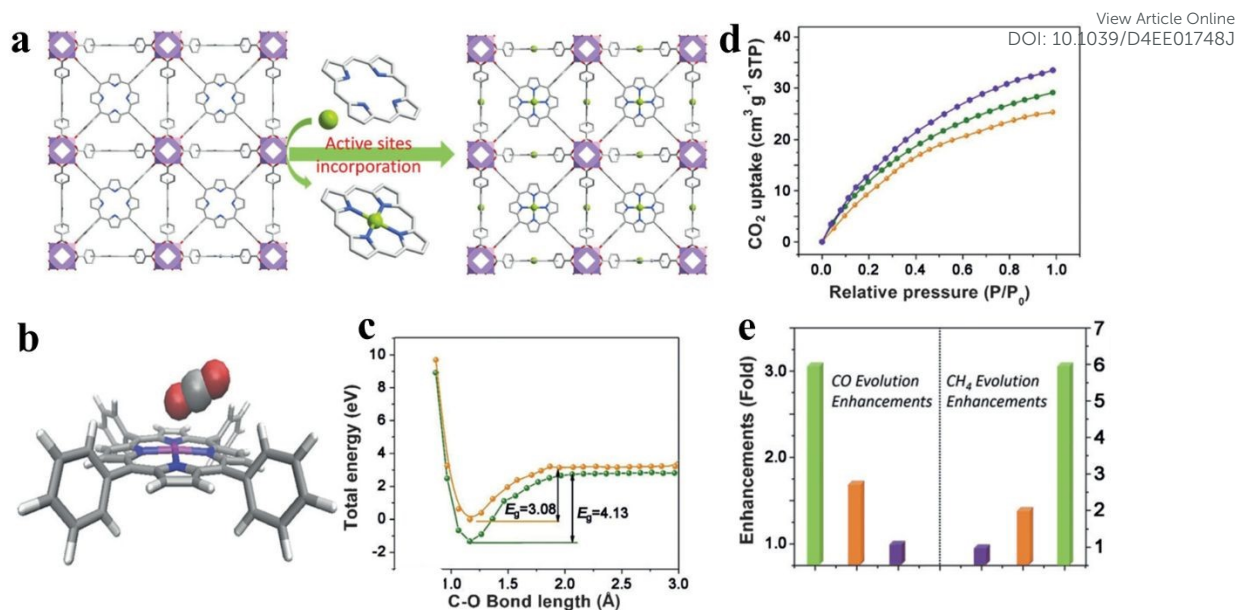


**Fig. 13.** (a) View of the 3D network of MOF-525-Co featuring a highly porous framework and incorporated active sites. (b) The optimized structure for CO<sub>2</sub> adsorption on a porphyrin-Co unit; (c) The O-C bond length-dependent CO<sub>2</sub> activation energy barrier, charged with one electron (orange), neutral state (green). (d) CO<sub>2</sub> adsorption behaviors for MOF-525 (orange) as well as MOF-525-Co (purple) and MOF-525-Zn (green) implanted with single atoms. (e) Enhancement of production evolution over MOF-525-Co (green), MOF-525-Zn (orange), and MOF-525-Zn (purple). Reproduced from ref.<sup>131</sup>. Copyright 2022 WILEY.

A heterojunction comprises dissimilar semiconductors with distinct electronic properties, most notably differing band gaps ( $E_g$ ). The band gap represents the energy difference between the valence band (VB) and the conduction band (CB), determining the minimum energy required for an electron to transition from the VB to the CB. In a heterojunction system, the semiconductors may have different chemical compositions, crystal structures, or dopant concentrations, resulting in varying  $E_g$  values and band edge positions. Its impact on photocatalysis is characterized by several key aspects: efficient charge separation, broadened light absorption, improved charge transport, interface catalytic effects. Ye and his team prepared Z-scheme photocatalyst consisting of PCN-224(Cu) and TiO<sub>2</sub> nanoparticles to improve the photocatalytic performance in CO<sub>2</sub> reduction. As **Fig. 14a**, TiO<sub>2</sub> and PCN-224(Cu) are intimately connected and generate a built-in electric field, under which photogenerated electrons migrate from the oxidizing side TiO<sub>2</sub> to the reducing side PCN-224(Cu).<sup>64</sup> Advanced structure of hybrid photocatalyst retains the original redox strength of the semiconductor and enhances the photoelectric absorption capability. As **Fig. 14b, c**, the light harvesting and light response of hybrid photocatalyst 15%P(Cu)/TiO<sub>2</sub> are obviously improved. The photocatalytic CO<sub>2</sub> reduction test was carried out in gas phase system without any sacrificial agent and photosensitizer. And the integration is capable of significantly triggering the improvement in photocatalytic CO<sub>2</sub> reduction into CO, with an evolution rate of 37.21  $\mu\text{mol g}^{-1} \text{h}^{-1}$ , which is 10 times and 45.5 times higher than that of pristine PCN-224(Cu) and pure TiO<sub>2</sub>, respectively (**Fig. 14d**).

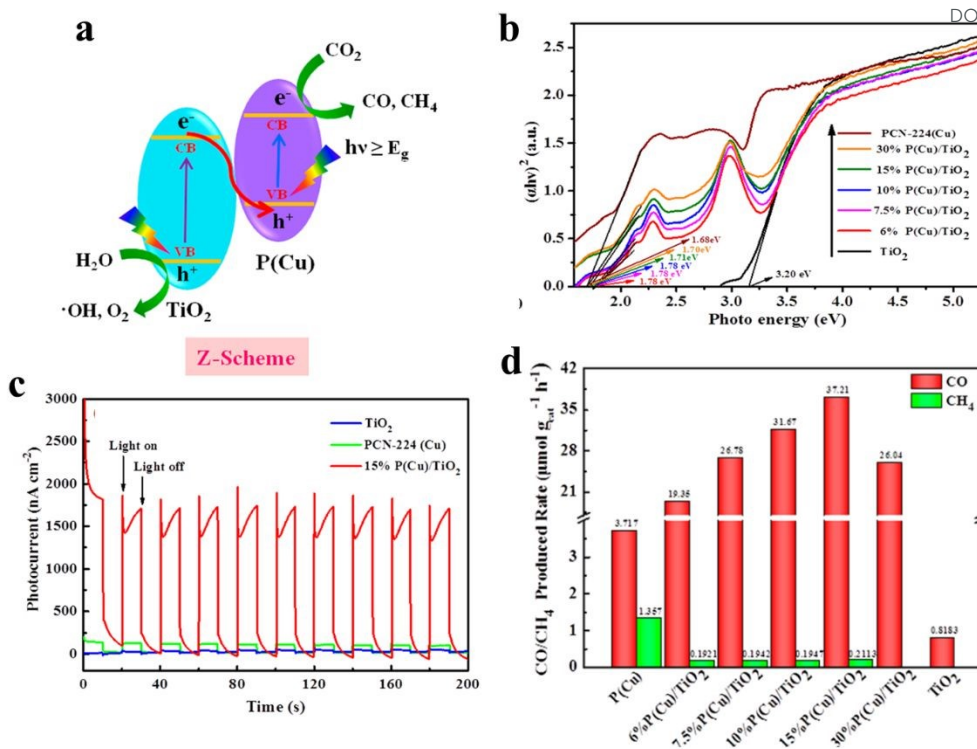


**Fig. 14.** (a) Direct Z-scheme photocatalytic mechanism. (b) energy band-gaps ( $E_g$ ) of TiO<sub>2</sub>, PCN-224(Cu), and PCN-224(Cu)/TiO<sub>2</sub>. (c) Photocurrent-time (I-t) curves of TiO<sub>2</sub>, PCN-224(Cu), and 15%P(Cu)/TiO<sub>2</sub> photoelectrodes at 0.6 V vs REH bias potential in 0.5 M Na<sub>2</sub>SO<sub>4</sub> (pH ~7.35). (d) CO and CH<sub>4</sub> generation velocity over PCN-224(Cu), 6%P(Cu)/TiO<sub>2</sub>, 7.5%P(Cu)/TiO<sub>2</sub>, 10%P(Cu)/TiO<sub>2</sub>, 15%P(Cu)/TiO<sub>2</sub>, 30%P(Cu)/TiO<sub>2</sub>, and TiO<sub>2</sub> under 300 W Xe lamps. Reproduced from ref. <sup>64</sup>. Copyright 2022 ACS.

The photocatalytic reduction of CO<sub>2</sub> offers a promising avenue for harnessing sunlight to convert the abundant greenhouse gas into valuable chemical commodities and fuels, all while operating under mild and energy-efficient conditions. This environmentally benign and potentially transformative technology has attracted significant attention, prompting numerous research endeavors aimed at enhancing the photocatalytic performance of porphyrin-based MOFs. These efforts are geared towards expediting the practical deployment of porphyrin MOFs as efficient photocatalysts for CO<sub>2</sub> reduction. This section provides an overview of how various synthetic strategies, metal active sites, configurations, single-atom doping, and heterojunction designs influence the chemical stability, product selectivity, photocatalytic activity, and photoelectrochemical properties of porphyrin-based MOFs. Subsequently, recent advances in applying these materials to the photocatalytic reduction of CO<sub>2</sub> are summarized in **Table 1**. IHEP-22(Co) shows the best performance of photocatalytic reduction of CO<sub>2</sub> to CO reaches 350.9  $\mu\text{mol}\cdot\text{h}^{-1}\cdot\text{g}^{-1}$ . The metal center not only serves as a pathway for the photogenerated electrons from porphyrin to transfer to CO<sub>2</sub> molecules, but also, through spatial regulation, it has been observed that the stacking method, spatial angle, and distance of porphyrin in MOFs greatly influence the photocatalytic conversion of CO<sub>2</sub>. The high modifiability of porphyrin-based MOFs allows for significant potential for future

research exploring the correlation between spatial structure and catalytic activity

View Article Online  
DOI: 10.1039/D4EE01748J

**Table 1.** The recent works of porphyrin-based MOFs applied in photocatalytic CO<sub>2</sub> reduction.

Samples	Porphyrins	Products	Performance ( $\mu\text{mol g}^{-1} \text{h}^{-1}$ )	Selectivity	Refs.
PCN-224(Cu)/TiO <sub>2</sub>	CuTCPP	CO/CH <sub>4</sub>	37.21/0.22	99.4%	64
In-Fe <sub>1.91</sub> TCPP-MOF	FeTCPP	CO/CH <sub>4</sub>	144/0.72	99.5%	129
In-Co <sub>1.71</sub> TCPP-MOF	CoTCPP	CO	38.1	-	129
In-InTCPP-MOF	InTCPP	CO	551	-	129
IHEP-22(Co)	CoTCPP	CO/CH <sub>4</sub>	350.9/8.9	97.5%	132
IHEP-22(Cu)	CuTCPP	CO/CH <sub>4</sub>	230/19.45	92.2%	132
MOF-525-Co	CoTCPP	CO/CH <sub>4</sub>	200.6/36.8	84.5%	131
g-C <sub>3</sub> N <sub>4</sub> /Cu-CuTCPP MOF	CuTCPP	CO/CH <sub>4</sub>	11.6/18.5	71%	133
Zn/PMOF	ZnTCPP	CH <sub>4</sub>	8.7	-	127
BUT-109(Zr)	DCPP	CO	22.6	-	128
BUT-110-50%-Co	DCPP	CO/CH <sub>4</sub>	64/11.3	85%	128
MOF 1(monolayer)	TPP	CO	60.9	100%	134
MOF 2 (bilayer)	TPP	CO	46.14	100%	134
g-CNQDs/PMOF	TCPP	CO/CH <sub>4</sub>	16.1/6.8	70.1%	135
Cu -PMOF	CuTCPP	HCOOH	130.6	-	136

## 5. Porphyrin-based MOFs for electrocatalytic CO<sub>2</sub> reduction

The CO<sub>2</sub>RR is typically conducted in a saturated aqueous sodium carbonate solution, organic solution, or ionic solution, under milder conditions compared to the hydrogen evolution reaction (HER), oxygen evolution reaction (OER), and oxygen reduction reaction (ORR) conducted in strong acidic and alkaline systems<sup>78, 137, 138</sup>. The integration of porphyrin-based MOFs has allowed for the transition of porphyrins from original homogeneous catalytic systems to heterogeneous catalytic systems<sup>127, 139, 140</sup>. Common products resulting from heterogeneous catalytic electrochemical CO<sub>2</sub>RR include CO, CH<sub>4</sub>, HCOO<sup>-</sup>, C<sub>2</sub>H<sub>4</sub>, among others.<sup>38, 75, 141</sup> However, research on the electrochemical CO<sub>2</sub>RR of porphyrin-based MOFs is limited due to challenges such as the competitive hydrogen precipitation reaction, low reaction efficiency, and poor selectivity<sup>142-144</sup>. Gu, *et al.* prepared copper(II) paddle wheel cluster-based porphyrinic metal-organic framework (MOF) nanosheets for electrochemical CO<sub>2</sub>RR. The discussion further examines the outstanding product selectivity and structural modifications of Cu<sub>2</sub>(CuTCPP) nanosheets.<sup>145</sup> As **Fig. 15a**, Cu-MOF nanosheets exhibit significant activity for formate production with a faradaic efficiency (FE) of 68.4% and acetate production with a FE of 16.8% under CO<sub>2</sub>-saturated CH<sub>3</sub>CN solution with 1 M H<sub>2</sub>O and 0.5 M EMIMBF<sub>4</sub>. By analyzing linear sweep voltammetry (LSV) curves of Cu<sub>2</sub>(CuTCPP), a significant amount of hydrogen was generated as a byproduct of the electrocatalytic process, and the changing trend of current density over time indicates the possibility of chemical restructuring of Cu<sub>2</sub>(CuTCPP) occurring after the first hour. Thus, the pre-electrolyzed Cu<sub>2</sub>(CuTCPP) nanosheets

was further used to eliminate the side reactions during the initial process and further confirm the activity of the final cathodized catalyst. At the appropriate working potential (-1.55V), the total FC of for formate and acetate formation reaches 85.2% (**Fig. 15b-e**). The excellent performance is mainly attributed to synergy between  $\text{Cu}_2(\text{CuTCPP})$  nanosheets and  $\text{CuO}$ ,  $\text{Cu}_2\text{O}$  and  $\text{Cu}_4\text{O}_3$ . In addition, the energy-states change after 5 h reaction for Cu species is reflected through XPS spectra, the peaks at 569.5 eV and 572.5 eV, which are ascribed to the kinetic energy of  $\text{Cu}^+$  and  $\text{Cu}^{2+}$ , respectively (**Fig. 15f, g**). The results indicate the instability of catalyst  $\text{Cu}_2(\text{CuTCPP})$  in the electrocatalytic  $\text{CO}_2\text{RR}$  process. However, the substitution of the catalyst resulted in an unforeseen impact on the catalytic process.

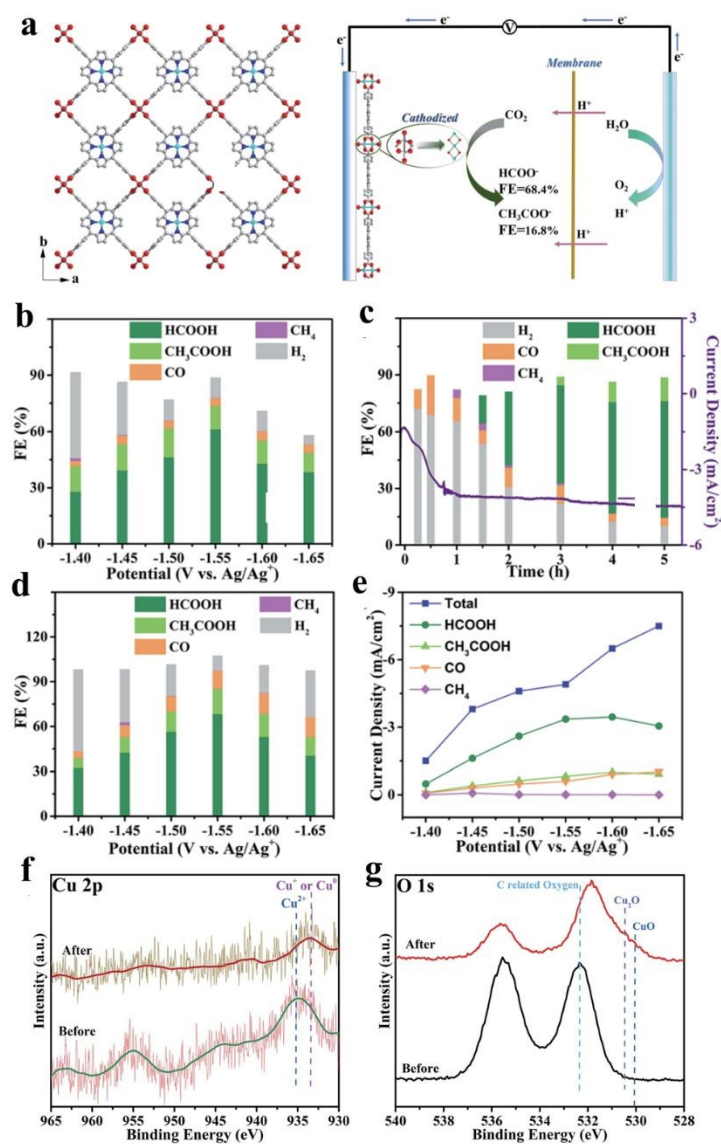


**Fig. 15.** (a) Crystal structure of  $\text{Cu}_2(\text{CuTCPP})$  nanosheets along the  $c$  axis. Red is O, blue is N, grey is C and cyan is Cu and  $\text{CO}_2$  electrochemical reduction system with  $\text{Cu}_2(\text{CuTCPP})$  nanosheets as the catalyst. (b) Faradaic efficiencies of  $\text{Cu}_2(\text{CuTCPP})$  nanosheets. (c) Faradaic efficiencies of  $\text{Cu}_2(\text{CuTCPP})$  nanosheets at different times. (d) Faradaic efficiencies of pre-



electrolyzed  $\text{Cu}_2(\text{CuTCPP})$  nanosheets. **(e)** Total and partial current densities for  $\text{CO}_2\text{RR}$  products on pre-electrolyzed  $\text{Cu}_2(\text{CuTCPP})$ . **(f)** Cu 2p XPS spectra and **(g)** O 1s XPS spectra of  $\text{Cu}_2(\text{CuTCPP})$  on FTO before and after 5 h reaction. All potentials were set at  $-1.55$  V vs.  $\text{Ag}/\text{Ag}^+$ . Reproduced from ref.<sup>145</sup>. Copyright 2022 RSC.

The manipulation and alteration of linkers in porphyrin-based metal-organic frameworks (MOFs) represent a strategic approach to tuning their electrical conductivity, thereby enhancing their electrochemical performance.<sup>53, 91, 126</sup> This is achieved through the introduction or substitution of functional linkers that facilitate charge transport while maintaining the inherent porphyrin topology.<sup>146</sup> Huang and his team integrated viologen groups into cobalt porphyrin (Por(Co))-based MOFs by self-assembly method for the first time to act as electron-transfer mediators (ETMs) to enhance the electron-transfer capacity and thus improve the activity of the  $\text{CO}_2\text{RR}$  (as **Fig. 16a**).<sup>147</sup> Interestingly, the groups both Vg and Por(Co) possess the similar length ( $19.65$  Å and  $19.62$  Å, respectively) and the same end functional group, which is benefit to form coordination bonds with the  $\text{Hf}_6\text{O}_8$  ( $\text{Zr}_6\text{O}_8$ ) cluster. And more positive onset potential and higher current densities in the  $\text{CO}_2$ -saturated  $0.5$  M  $\text{KHCO}_3$  solution demonstrate outstanding reaction activity and feasibility of the  $\text{CO}_2\text{RR}$ , according to the LSV curves (**Fig. 16b, c**). Then, Vg-Por(Co)-MOF ( $n : 1$ ) ( $n = 1, 3, 5, 9$ ) show lower potential under the current density of  $10$   $\text{mA g}^{-1}$  indicated the more electron transfer efficiency than pure Vg-MOF and Por(Co)-MOF. And compared with other components, the Vg-Por(Co)-MOF ( $9 : 1$ ) exhibited the best activity in the  $\text{CO}_2\text{RR}$  with  $j_{\text{CO}}$  of  $24.3$   $\text{mA cm}^{-2}$  at  $-1.0$  V and a high  $\text{FE}_{\text{CO}}$  of  $93.7\%$  at  $-0.6$  V (**Fig. 16d**). Finally, a long term electrocatalytic test at a fixed potential of  $-0.6$  V indicate that Vg-Por(Co)-MOF ( $9 : 1$ ) owns a electrochemical stability for  $\text{CO}_2\text{RR}$  (**Fig. 16e**).

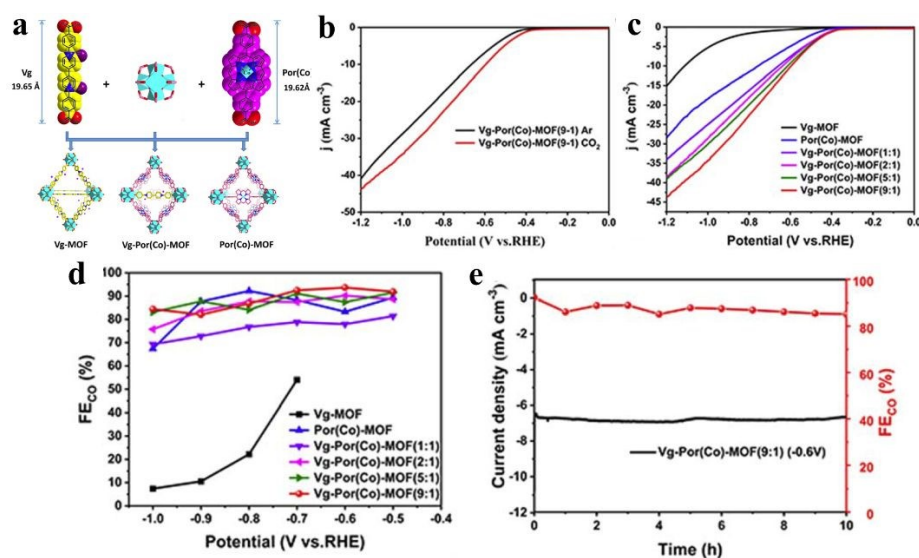


**Fig. 16.** **(a)** Schematic synthesis diagram for Vg-MOF, Por(Co)-MOF, and Vg-Por(Co)-MOF by solvothermal method. **(b)** LSV curves of Vg-Por(Co)-MOF ( $9 : 1$ ) in  $\text{CO}_2$ - and Ar-saturated  $0.5$  M  $\text{KHCO}_3$ . **(c)** LSV curves of Vg-MOF, Por(Co)-MOF and Vg-Por(Co)-MOF ( $n : 1$ ) ( $n = 1, 2, 5, 9$ ) in  $0.5$  M  $\text{KHCO}_3$  electrolyte under  $\text{CO}_2$ . **(d)** Faradaic efficiencies of CO for Vg-MOF, Por(Co)-MOF and Vg-Por(Co)-MOF ( $n : 1$ ) ( $n = 1, 3, 5, 9$ ). **(e)** Stability of Vg-Por(Co)-MOF ( $9 : 1$ ) at a

potential of -0.6 V versus RHE for 10 h. Reproduced from ref. <sup>147</sup>. Copyright 2022 RSC. [View Article Online](#)  
DOI: 10.1039/D4EE01748J

Selectivity is indeed a critical challenge in the electrocatalytic reduction of carbon dioxide (CO<sub>2</sub>RR) as it determines the efficiency of converting CO<sub>2</sub> into valuable chemical feedstocks and fuels.<sup>21, 41, 44, 49</sup> A novel strategy to enhance the selectivity of porphyrin-based MOFs for CO<sub>2</sub>RR involves the careful modification of cationic groups within the MOF structure to stabilize specific reaction intermediates. This approach capitalizes on the intrinsic properties of porphyrin MOFs and tailors their electrochemical environment to favor desired product formation.<sup>42</sup> Hod *et al.* prepared Fe-porphyrin (Hemin)-modified Zr<sub>6</sub>-oxo based 2D-MOF (Zr-BTB@Hemin) for electrocatalytic CO<sub>2</sub>RR, owing to the porous, robust structure and mass transport<sup>78</sup>. However, Unsatisfied catalytic activity and product selectivity are the drawbacks for Zr-BTB@Hemin to be applied in CO<sub>2</sub>RR. In this case, authors tethered a cationic functional group, (3-carboxypropyl)trimethylammonium (TMA) proximal to the Fe-porphyrin active site via post-synthesis (Zr-BTB@Hemin-TMA). The details of synthesis processes and catalyst's structure can be found in **Fig. 17a**. As shown in **Fig. 17c, d**, Zr-BTB@Hemin-TMA exhibit higher electrochemical activity under CO<sub>2</sub> atmosphere and more outstanding CO product selectivity (about 92 %, at the potential of 1.2 V vs. NHE) than that without TMA group, which is mainly attributed to electrostatic stabilization of a weakly-bound CO intermediate, which accelerated its release as a catalytic product. In order to obtain the detail insights on the mechanisms governing the improved electrocatalytic CO<sub>2</sub>-to-CO performance of Zr-BTB@Hemin-TMA compared to Zr-BTB@Hemin, Raman spectroscopy test was carried out reveal the possible electronic communication between MOF-installed Hemin and TMA ligands. The peaks of Zr-BTB@Hemin at 1367 cm<sup>-1</sup> and 1562 cm<sup>-1</sup> shift to 1369 cm<sup>-1</sup> and 1568 cm<sup>-1</sup> after being modified by TMA, which means the conversion of low-spin Fe<sup>3+</sup>-Hemin into a high-spin species (**Fig. 17g, h**). Then, *in-situ* Raman measurements were performed at a set of applied potentials (1.1 to 1.6 V vs. NHE) under CO<sub>2</sub> reduction conditions. Compared to Zr-BTB@Hemin, the intensity of 2060 cm<sup>-1</sup> peak of Zr-BTB@Hemin-TMA is larger than that of the one at 1840 cm<sup>-1</sup>, which means a stabilizes intermediate CO with weak bonds, allowing for swift release of the CO product (**Fig. 17e, f**). The conclusion is reinforced by the bonding mode illustrated at the peak of 2060 cm<sup>-1</sup> and 1840 cm<sup>-1</sup> in **Fig. 17b**. Thus, electrostatic secondary-sphere functionalities enable substantial improvement of CO<sub>2</sub>-to-CO conversion activity and selectivity.

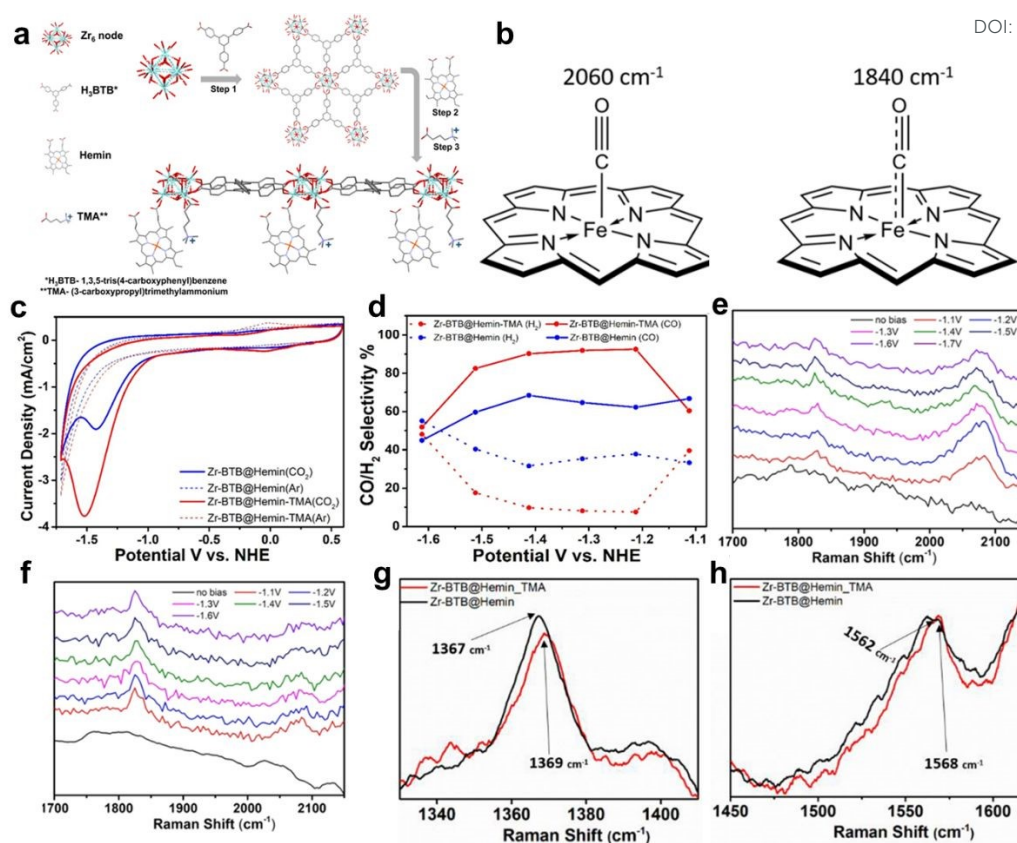


**Fig. 17.** (a) Schematic illustration of Zr-BTB@Hemin-TMA synthesis. Step 1, showing the preparation of Zr-BTB nanosheet. Step 2, post-synthetic modification with Hemin (molecular catalyst). Step 3, post-synthetic modification with TMA (electrostatic secondary-sphere ligand). (b) Schematic illustration showing the different C-O and Fe-C bond orders for the 2 Hemin-bound CO intermediates detected using *in-situ* Raman spectroscopy. (c) Cyclic voltammetry measurements comparing Zr-BTB@Hemin (blue), and Zr-BTB@Hemin-TMA (red) in both Ar (dashed line) and CO<sub>2</sub> environment (solid line). (d) Comparison of catalytic selectivity towards CO (solid line) and H<sub>2</sub>(dashed line) for Zr-BTB@Hemin (blue) Zr-BTB@Hemin-TMA (red). (e-f) *In-situ* Raman spectroscopy measurements conducted under working electrocatalytic conditions; The Raman spectra of Zr-BTB@Hemin (black) and Zr-BTB@Hemin\_TMA (red). (g) Expansion of the region showing the v<sub>4</sub> peak of the pyrrole half-ring stretching. (h) Expansion of the region showing the v<sub>2</sub> peak region of the pyrrole half-ring stretching. Reproduced from ref. <sup>78</sup>. Copyright 2022 WILEY.

The porphyrin moiety in porphyrin-based MOFs is characterized by a highly stable, planar, aromatic ring structure adorned with 18 electron  $\pi$ -bonds.<sup>41, 56, 60, 148</sup> Despite the inherent stability and unique electronic properties of porphyrins, the majority of research efforts have focused on utilizing composite catalyst systems to enhance the electrical conductivity and cyclic stability of these MOFs<sup>149</sup>. This is often achieved by introducing additional components that can establish weak  $\pi$ - $\pi$  interactions with the porphyrin rings.<sup>76</sup> While such interactions can marginally improve the electrical performance of the hybrid material, they fall short of fully exploiting the potential electrical conductivity offered by the porphyrin-based MOF. To truly unlock the full photoelectric potential of these complexes, direct coordination

of the porphyrin core with suitable ligands or dopants becomes essential. Mu and her team created a porphyrin-based Cu MOFs (Cu-(Co + Cu)PMOF/CNT-COOH hybrid) by integrating a two-dimensional bimetallic porphyrin-based Cu-MOF with carboxyl-modified carbon nanotubes (**Fig. 18a, b**).<sup>150</sup> (Co + Cu)PMOF/CNT without carboxyl-modified, which is formed through weak  $\pi$ - $\pi$  interaction between (Co + Cu)PMOF and carbon nanotube (CNT). However, In sharp contrast, Cu-(Co + Cu)PMOF/CNT-COOH shows superior stability, additional exposed active sites, and a higher electron transfer rate from CNT-COOH to Cu-(Co + Cu)PMOF (**Fig. 18c**) and achieves a CO faradic efficiency of 95.98% with an impressive current density of  $-3.48 \text{ mA cm}^{-2}$  at an overpotential of  $-0.9 \text{ V}$  vs. RHE. Then, a stability test of 40000 s further demonstrate a super stability of Cu-(Co + Cu)PMOF/CNT-COOH (**Fig. 18d-f**). As we know,  $\text{C}_{2+}$  products, derived predominantly from petroleum, are fundamental chemicals widely used in industries such as plastics, synthetic fibers, and solvents.<sup>151</sup> However, their production via electrocatalytic  $\text{CO}_2$  reduction is hampered by kinetic barriers and inefficiencies in proton/electron transfer, particularly concerning the challenging C-C coupling reactions.<sup>152</sup> Porphyrin-based Cu MOFs have garnered significant attention in the field of electrocatalytic  $\text{CO}_2$ -to- $\text{C}_{2+}$  products, primarily due to the unique advantage that the Cu coordination environment can be finely tuned through adjusting Cu-N interactions. This precise modulation of the electronic properties of Cu active site enables porphyrin-based Cu MOFs to exhibit enhanced selectivity towards  $\text{C}_{2+}$  products. Nonetheless, sluggish kinetics and inefficient mass transport remain as formidable challenges impeding the full realization of their potential in this application<sup>153</sup>. Yang and his team successfully synthesized Porphyrin-based Cu MOFs comprising metalloporphyrin Cu centers and impregnated Au nanoneedles by exploiting the ligand carboxylates as the reducing agent (AuNN@PCN-222(Cu)).<sup>154</sup> AuNN@PCN-222(Cu) demonstrated significantly improved ethylene production up to an FE of 52.5%. the satisfied FE was mainly attributed to the Cu- $\text{N}_4$  motif undergoes an out-of-plane displacement toward the Au plane, freeing the Cu center to accept another Au-generated CO in affording the co-adsorption of  $\ast\text{CO}$  and  $\ast\text{CHO}$  with an exothermic energy difference of  $-0.08 \text{ eV}$ . Subsequently, C-C coupling occurs by bridging the two intermediates to form  $\ast\text{CO-CHO}$  with a surmountable energy of  $0.44 \text{ eV}$ . The presence of co-adsorption sites has been demonstrated to lower the energy barrier for C-C coupling while concurrently enhancing mass transfer efficiency, thereby capitalizing on copper's versatile valence properties. This strategic approach holds instructive value for future investigations into electrocatalytic  $\text{CO}_2$ -to- $\text{C}_{2+}$  products, guiding the design of more efficient and selective catalyst systems.

View Article Online  
DOI: 10.1039/D4EE01748J

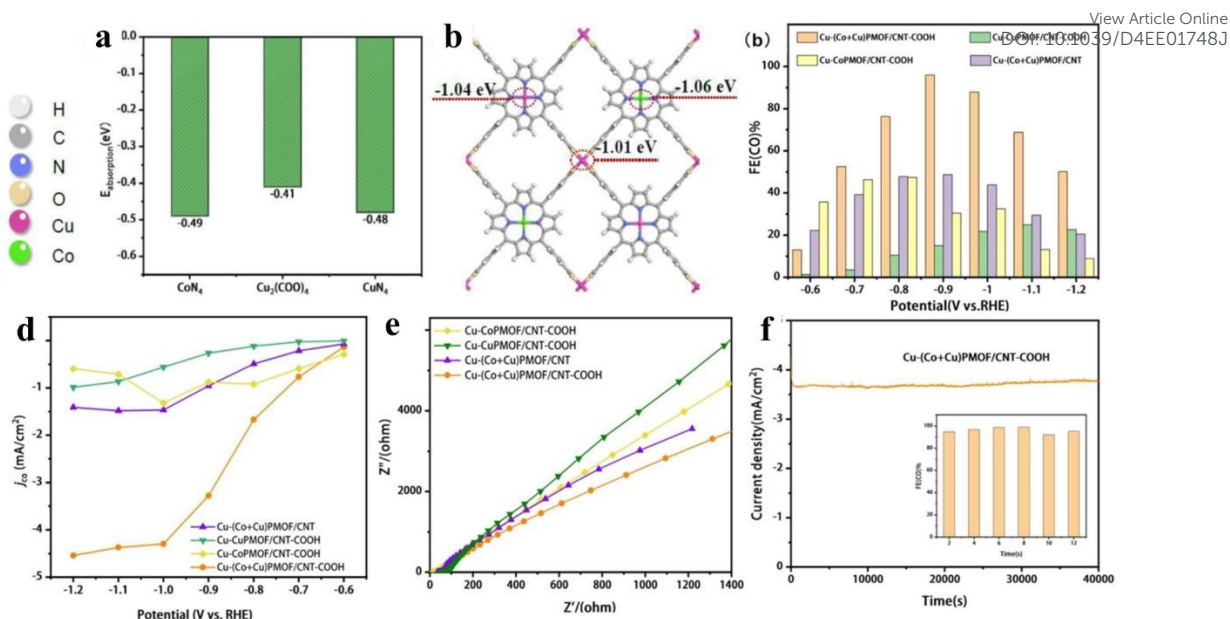


**Fig. 18.** (a) adsorption energies of  $\text{CO}_2$  on  $\text{Cu}_2(\text{COO})_4$ ,  $\text{CoN}_4$  and  $\text{CuN}_4$  sites. (b) Bader charge of  $\text{Cu}_2(\text{COO})_4$ ,  $\text{CuN}_4$  and  $\text{CoN}_4$  sites on  $\text{Cu}-(\text{Cu} + \text{Co})\text{PMOF}$ . (c) Faradaic efficiency for CO and (d) CO partial current density of  $\text{Cu}-\text{CoPMOF}/\text{CNT}-\text{COOH}$ ,  $\text{Cu}-\text{CuPMOF}/\text{CNT}-\text{COOH}$ ,  $\text{Cu}-(\text{Co} + \text{Cu})\text{PMOF}/\text{CNT}$  and  $\text{Cu}-(\text{Co} + \text{Cu})\text{PMOF}/\text{CNT}-\text{COOH}$  at different potentials (-0.6 ~ -1.2 V vs. RHE). (e) Nyquist plots of  $\text{Cu}-\text{CuPMOF}/\text{CNT}-\text{COOH}$ ,  $\text{Cu}-\text{CoPMOF}/\text{CNT}-\text{COOH}$ ,  $\text{Cu}-(\text{Co} + \text{Cu})\text{PMOF}/\text{CNT}-\text{COOH}$  and  $\text{Cu}-(\text{Co} + \text{Cu})$ . (f) Long-term stability test of  $\text{Cu}-(\text{Co} + \text{Cu})\text{PMOF}/\text{CNT}-\text{COOH}$  at -0.9 V for 12 h. Reproduced from ref. <sup>150</sup>. Copyright 2022 ELSEVIER.

Electrocatalytic  $\text{CO}_2\text{RR}$  holds great promise in transforming the greenhouse gas  $\text{CO}_2$  into valuable chemicals and fuels, contributing to both environmental sustainability and resource utilization. Porphyrin-based metal-organic frameworks (MOFs) have emerged as intriguing candidates for this purpose, given their unique structural versatility, tunable porosity, and rich redox chemistry.<sup>44, 61, 148</sup> Nevertheless, the practical implementation of porphyrin MOFs as efficient electrocatalysts for  $\text{CO}_2\text{RR}$  necessitates improvements in several critical aspects, including product selectivity, cycle stability, conductivity, and catalytic activity. Recognizing the potential of these materials, substantial research efforts have been dedicated to optimizing porphyrin MOFs for the high-value conversion of  $\text{CO}_2$ . This section elucidates how the stability, selectivity, and conductivity of porphyrin-based electrocatalysts can be meticulously tailored through judicious manipulation of the surrounding groups, porphyrin metal centers, and diverse porphyrin linkers. Finally, efforts the recent works about applying porphyrin-based MOFs to the electrocatalytic  $\text{CO}_2$  reduction (**Table 2**). Notably, MOF-NS-Co demonstrates remarkable activity in electrocatalytic  $\text{CO}_2$  reduction, with the CO Faradaic efficiency of MOF-NS-Co surpassing 90% across a broad potential range of -0.5 to -1.0 V, peaking at 98.7% with a mere 100 mV increment. This outstanding performance can be attributed to the unique a Kagome-type layer pillared structure of the porphyrin-based MOFs, which exposes a high density of active metal sites and lowers the energy barrier for the generation and conversion of intermediates in the  $\text{CO}_2$  reaction.

**Table 2.** The recent works of porphyrin-based MOFs applied in electrocatalytic CO<sub>2</sub>RR. View Article Online  
DOI: 10.1039/D4EE01748J

Samples	Porphyrins	Products	Electrolyte	FE and E <sub>on set</sub> (V vs. RHE)	Refs.
Cu-porphyrin MOF	CuTCPP	C <sub>2</sub> H <sub>5</sub> OH/C <sub>2</sub> H <sub>4</sub> / CH <sub>4</sub> /CO	0.1 M KHCO <sub>3</sub>	11.9% to 41.1% at -1.4 V	155
g-C <sub>3</sub> N <sub>4</sub> @Co- (Co + Cu)PMOF-50% MOF-525	TCPP CoTCPP	CO CH <sub>4</sub> /CO	0.1 M 0.1 M KHCO <sub>3</sub>	97.8% at -1.4 V 87% at -0.89 V	156 150
MOF-NS-Co	TCPP	CO	0.1 M KHCO <sub>3</sub>	98.7% at -0.6 V	157
Al <sub>2</sub> (OH) <sub>2</sub> TCPP-Co	CoTCPP	CO	0.5 M KHCO <sub>3</sub>	76% at -0.7 V	158
TCPP(Co)/Zr-BTB- PSABA 2D Cu-MOF	CoTCPP CuTCPP	CO CH <sub>3</sub> COOH/ HCOOH/ CO/CH <sub>4</sub>	0.5 M 0.5 M 1 M H <sub>2</sub> O and 0.5 M EMIMBF <sub>4</sub>	85.1% at -0.77 V 16.8% and 68.4% at -1.55 V <sub>Ag/Ag+</sub>	87 159
PPy@MOF-545-Co	CoTCPP	CO	0.5 M KHCO <sub>3</sub>	98% at -0.8 V	96
PPy@MOF-545-Fe	FeTCPP	CO	0.5 M KHCO <sub>3</sub>	89.2% at -0.7 V	96
PPy@MOF-545-Ni	NiTCPP	CO	0.5 M KHCO <sub>3</sub>	87.8% at -0.9 V	96
Fe-Porphyrin (Hemin)-based MOF	Hemin	CO	0.5 M KHCO <sub>3</sub>	92 % at -1.2 V	78
PCN-222(Fe)/C	FeTCPP	CO	0.5 M KHCO <sub>3</sub>	80.4% at -0.6 V	41
Vg-Por(Co)-MOF(9 : 1)	DPDBP	CO	0.5 M KHCO <sub>3</sub>	93.8% at 2.3 V	44

## 6. Conclusions and outlook

Porphyrin-based MOFs have recently emerged as promising candidates for photo(electro)catalytic CO<sub>2</sub> conversion reactions due to their straightforward synthesis, high chemical stability, abundant metallic active sites, tunable crystalline structure, and high specific surface area. This review comprehensively discusses the fundamentals of porphyrin-based MOFs and their derivative catalysts for valuable CO<sub>2</sub> conversion, covering topics such as synthesis, catalytic mechanisms, and strategies for enhancing photo(electro)catalytic CO<sub>2</sub> reduction. The potential of porphyrin-based MOFs in this field is clearly demonstrated. Despite significant progress in recent years, further research is needed to fully explore the capabilities of porphyrin-based MOFs in photo(electro)catalytic CO<sub>2</sub> reduction. Several challenges and bottlenecks remain to be addressed.

(i) One major obstacle in photocatalytic and electrocatalytic reduction of CO<sub>2</sub> is the low selectivity towards desired products, as HER also occur simultaneously. While the Fischer-Tropsch process can potentially convert CO<sub>2</sub> and H<sub>2</sub> into hydrocarbons, it does not address the selectivity problem and adds an energy-intensive conversion step. Thus, improving the direct selectivity of CO<sub>2</sub> reduction processes is essential for their practical implementation.

(ii) The pursuit of a cost-effective and efficient porphyrin-based MOFs catalyst as an alternative to noble metal catalysts in CO<sub>2</sub> reduction encounters various challenges. Additionally, the practical application of photo(electro)catalytic CO<sub>2</sub>RR is impeded by the intricate processes involved in their synthesis, processing, and less than ideal photo(electro)chemical properties. These obstacles necessitate extensive research and development endeavors in this field, which are both technically complex and financially taxing.

(iii) Long-term stable operation is a crucial requirement for any practical catalyst. Porphyrin-based MOFs are susceptible to structural degradation, loss of active components, pore blockage, and other issues during actual operation, which can impact their catalytic efficiency and lifespan. It is essential to develop new MOF materials with superior corrosion resistance and structural stability, along with researching suitable packaging techniques and anti-aging methods, to enhance their long-term stability in real-world applications.

(iv) Although porphyrin-based MOFs have shown promising CO<sub>2</sub>RR performance in laboratory settings, challenges such as high production costs, limited feedstock availability, and process complexity hinder their commercialization. To overcome these barriers, it is crucial to focus on streamlining synthetic routes, utilizing cost-effective feedstocks, implementing continuous production methods, and enhancing recycling strategies. These efforts are key to reducing costs, enhancing resource efficiency, and facilitating industrial-scale production.

Despite the development bottlenecks mentioned above, we will find appropriate strategies to address these issues as we continue to explore them.

(i) The reaction pathway for CO<sub>2</sub> catalysis is complicated, and the catalytic selectivity of porphyrin-based MOFs can be improved by precisely controlling the catalytic environment. Firstly, the presence of a substantial quantity of evenly distributed metal-active centers in porphyrin-based MOFs is a significant factor in the absorption and stabilization of CO<sub>2</sub> intermediates, as well as the selective desorption of products. Secondly, Porphyrin ligands are functionalized molecules. Choosing the suitable porphyrin ligands and integrating them into MOFs can greatly enhance selectivity. Finally, the configuration of the pore structure plays a major role in stabilizing reaction intermediates and facilitating their specific passage.

(ii) The porphyrin organic linkers' interaction with the metal nodes of porphyrin-based MOFs significantly affects their electrical conductivity. In porphyrin-based MOFs, metal nodes typically function as electron acceptors, while porphyrin ligands act as electron donors. Therefore, introducing a guest molecule to regulate the band gap structure formed between the electron donor and acceptor greatly impacts the photoelectrochemical performance.

(iii) Some common noble metal industrial catalysts remain active for at least 2400 h to reduce production costs. Although most of the current porphyrin-based MOFs catalysts demonstrate high CO<sub>2</sub> conversion efficiency, their stability studies necessitate extensive efforts. Therefore, long-term stability test is crucial. Current approaches to tackling the catalytic stability issues of porphyrin-based MOFs primarily include introducing robust linkers to enhance structural integrity,

incorporating protective groups to shield sensitive sites against degradation, and designing hybrid structures that synergistically merge the advantages of both organic and inorganic components. Furthermore, the dynamic restructuring of these catalysts during the catalytic cycle has been shown to significantly augment their longevity, thereby holding promise for achieving industrially relevant operational lifetimes in the future. The superb catalytic stability means that porphyrin-based MOFs will be more cost-effective for future applications in photocatalytic CO<sub>2</sub> reduction.

(iv) The adsorption capacity of porphyrin-based MOFs can effectively enhance the catalytic conversion efficiency of CO<sub>2</sub> within the catalytic system. For instance, increasing the local CO<sub>2</sub> concentration in the catalytic active center can improve the reaction yield and selectivity. Furthermore, porphyrin-based MOFs with high CO<sub>2</sub> adsorption selectivity can exhibit high catalytic activity in mixed gas or low CO<sub>2</sub> concentration or partial pressure environments.

In light of current research on porphyrin-based MOFs, this study suggests key areas for future exploration in the field of porphyrin-based MOFs photo(electro)catalytic CO<sub>2</sub> reduction. Specifically, investigating the potential enhancement of photocatalytic CO<sub>2</sub> activity through photoelectric synergy and understanding its underlying mechanisms are essential. The modifiable nature of porphyrin MOFs presents an opportunity to explore how steric structures can impact product selectivity. Furthermore, exploring various forms of metal active sites (such as single atoms, multi-metal atoms, and central coordination) in conjunction with steric effects could lead to the production of complex multi-carbon products. This area of research is poised to become a significant focus in the future. In conclusion, porphyrin-based MOFs show great potential as a photo(electro)catalytic material with a wide range of applications in CO<sub>2</sub> reduction. Continuous research and novation in this field will undoubtedly contribute significantly towards resolving global energy and environmental challenges.

### Acknowledgements

This work was supported by the National Natural Science Foundation of China (Grant No. 52203110) and the Natural Science Foundation of Fujian Province (Grant No. 2023J05052). Dedicated to Professor Geoffrey Ozin on the occasion of his 80th birthday.

### Conflicts of interest

There are no conflicts of interest to declare.



## Reference

View Article Online  
DOI: 10.1039/D4EE01748J

1. X. Jiao, K. Zheng, L. Liang, X. Li, Y. Sun and Y. Xie, *Chem. Soc. Rev.*, 2020, **49**, 6592-6604.
2. G. Ding, C. Li, Y. Ni, L. Chen, L. Shuai and G. Liao, *EES Catal.*, 2023, **1**, 369-391.
3. F. Tian, X. Wu, J. Chen, X. Sun, X. Yan and G. Liao, *Dalton Trans.*, 2023, **52**, 11934-11940.
4. G. Ding, Z. Wang, J. Zhang, P. Wang, L. Chen and G. Liao, *EcoEnergy*, 2024, **2**, 22-44.
5. G. Liao, Y. He, H. Wang, B. Fang, N. Tsubaki and C. Li, *Device*, 2023, **1**, 100173.
6. L. Tan, S. M. Xu, Z. Wang, Y. Xu, X. Wang, X. Hao, S. Bai, C. Ning, Y. Wang, W. Zhang, Y. K. Jo, S. J. Hwang, X. Cao, X. Zheng, H. Yan, Y. Zhao, H. Duan and Y. F. Song, *Angew. Chem. Int. Ed.*, 2019, **58**, 11860-11867.
7. L. Tan, S. M. Xu, Z. Wang, Y. Xu, X. Wang, X. Hao, S. Bai, C. Ning, Y. Wang, W. Zhang, Y. K. Jo, S. J. Hwang, X. Cao, X. Zheng, H. Yan, Y. Zhao, H. Duan and Y. F. Song, *Angew. Chem. Int. Ed.*, 2019, **58**, 11860-11867.
8. G. Liao, G. Ding, B. Yang and C. Li, *Precis. Chem.*, 2024, **2**, 49-56.
9. R. R. Ikreedeegh and M. Tahir, *J. CO<sub>2</sub> Util.*, 2021, **43**, 101381.
10. Q. Zhang, G. Liao, B. Yang, Y. Zhang, G. Ge, A. Lipovka, J. Liu, R. D. Rodriguez, X. Yang and X. Jia, *Appl. Surf. Sci.*, 2023, **638**, 157989.
11. X. Wang, S. Sahoo, J. Gascon, M. Bragin, F. Liu, J. Olchowski, S. Rothfarb, Y. Huang, W. Xiang, P.-X. Gao, S. P. Alpay and B. Li, *Energy Environ. Sci.*, 2023, **16**, 4388-4403.
12. E. V. Kondratenko, G. Mul, J. Baltusaitis, G. O. Larrazábal and J. Pérez-Ramírez, *Energy Environ. Sci.*, 2013, **6**, 3112-3135.
13. T. Yan, X. Chen, L. Kumari, J. Lin, M. Li, Q. Fan, H. Chi, T. J. Meyer, S. Zhang and X. Ma, *Chem. Rev.*, 2023, **123**, 10530-10583.
14. B. Chang, H. Pang, F. Raziq, S. Wang, K.-W. Huang, J. Ye and H. Zhang, *Energy Environ. Sci.*, 2023, **16**, 4714-4758.
15. Y. Zhang, B. Xia, J. Ran, K. Davey and S. Z. Qiao, *Adv. Energy Mater.*, 2020, **10**, 1903879.
16. A. Kumar Singh, C. Das and A. Indra, *Coordin. Chem. Rev.*, 2022, **465**, 214516.
17. Z. Wang, G. Ding, J. Zhang, X. Lv, P. Wang, L. Shuai, C. Li, Y. Ni and G. Liao, *Chem. Commun.*, 2024, **60**, 204-207.
18. B. Yang, X. Li, Q. Zhang, X. Yang, J. Wan, G. Liao, J. Zhao, R. Wang, J. Liu, R. D. Rodriguez and X. Jia, *Appl. Catal. B: Environ.*, 2022, **314**, 121521.
19. C. Li, B. Cheng, H. Lu, G. Ding, Z. Jiang and G. Liao, *Inorg. Chem.*, 2023, **62**, 6843-6850.
20. C. Li, X. Liu, G. Ding, P. Huo, Y. Yan, Y. Yan and G. Liao, *Inorg. Chem.*, 2022, **61**, 4681-4689.
21. S. Bai, C. Ning, H. Wang, G. Liu, L. Zheng and Y. F. Song, *Small*, 2022, **18**, e2203787.
22. B. Yang, Z. Wang, J. Zhao, X. Sun, R. Wang, G. Liao and X. Jia, *Int. J. Hydrogen Energy*, 2021, **46**, 25436-25447.
23. H. Zhu, C. Zhang, K. Xie, X. Li and G. Liao, *Chem. Eng. J.*, 2023, **453**, 139775.
24. G. Liao, C. Li, S.-Y. Liu, B. Fang and H. Yang, *Phys. Rep.*, 2022, **983**, 1-41.
25. C. Li, H. Lu, G. Ding, Q. Li and G. Liao, *Catal. Sci. Technol.*, 2023, **13**, 2877-2898.
26. G. Liao, C. Li, S.-Y. Liu, B. Fang and H. Yang, *Trends Chem.*, 2022, **4**, 111-127.

27. H. Zhu, L. Gou, C. Li, X. Fu, Y. Weng, L. Chen, B. Fang, L. Shuai and G. Liao, *Device*, 2024, **2**, 100283. View Article Online  
DOI: 10.1039/D4EE01748J
28. Y. Bo, P. Du, H. Li, R. Liu, C. Wang, H. Liu, D. Liu, T. Kong, Z. Lu, C. Gao and Y. Xiong, *Appl. Catal. B: Environ.*, 2023, **330**, 122667.
29. G. Liao, Y. Gong, L. Zhang, H. Gao, G.-J. Yang and B. Fang, *Energy Environ. Sci.*, 2019, **12**, 2080-2147.
30. M. Li, Z. Zuo and S. Zhang, *ACS Catal.*, 2023, **13**, 11815-11824.
31. G. Liao, L. Zhang, C. Li, S.-Y. Liu, B. Fang and H. Yang, *Matter*, 2022, **5**, 3341-3374.
32. M. Yang, P. Wang, Y. Li, S. Tang, X. Lin, H. Zhang, Z. Zhu and F. Chen, *Appl. Catal. B: Environ.*, 2022, **306**, 121065.
33. G. Marcandalli, K. Boterman and M. T. M. Koper, *J. Catal.*, 2022, **405**, 346-354.
34. M. C. O. Monteiro, F. Dattila, N. López and M. T. M. Koper, *J. Am. Chem. Soc.*, 2022, **144**, 1589-1602.
35. G. Marcandalli, M. C. O. Monteiro, A. Goyal and M. T. M. Koper, *Acc. Chem. Res.*, 2022, **55**, 1900-1911.
36. A. Schoedel, Z. Ji and O. M. Yaghi, *Nat. Energy*, 2016, **1**, 16034.
37. C. I. Ezugwu, S. Liu, C. Li, S. Zhuiykov, S. Roy and F. Verpoort, *Coordin. Chem. Rev.*, 2022, **450**, 214245.
38. B. Zhu, Q. Xu, X. Bao, H. Yin, Y. Qin and X.-C. Shen, *Chem. Eng. J.*, 2022, **429**, 132284.
39. C. Li, G. Ding, X. Liu, P. Huo, Y. Yan, Y. Yan and G. Liao, *Chem. Eng. J.*, 2022, **435**, 134740.
40. C. Li, X. Liu, P. Huo, Y. Yan, G. Liao, G. Ding and C. Liu, *Small*, 2021, **17**, 2102539.
41. B.-X. Dong, S.-L. Qian, F.-Y. Bu, Y.-C. Wu, L.-G. Feng, Y.-L. Teng, W.-L. Liu and Z.-W. Li, *ACS Appl. Energy Mater.*, 2018, **1**, 4662-4669.
42. Y. Chen, D. Wang, X. Deng and Z. Li, *Catal. Sci. Technol.*, 2017, **7**, 4893-4904.
43. Y. Qiao, C. Sun, J. Jian, T. Zhou, X. Xue, J. Shi, L. Zhao and G. Liao, *Inorg. Chem.*, 2024, **63**, 2060-2071.
44. Y.-L. Dong, Z.-Y. Jing, Q.-J. Wu, Z.-A. Chen, Y.-B. Huang and R. Cao, *J. Mater. Chem. A*, 2023, **11**, 8739-8746.
45. X. Duan, J. Xu, Z. Wei, J. Ma, S. Guo, S. Wang, H. Liu and S. Dou, *Adv. Mater.*, 2017, **29**, 1701784.
46. X. J. Kong, T. He, J. Zhou, C. Zhao, T. C. Li, X. Q. Wu, K. Wang and J. R. Li, *Small*, 2021, **17**, e2005357.
47. C. Li, W. Qiu, W. Long, F. Deng, G. Bai, G. Zhang, X. Zi and H. He, *J. Mol. Catal. A: Chem.*, 2014, **393**, 166-170.
48. R. J. Li, M. Li, X. P. Zhou, D. Li and M. O'Keeffe, *Chem. Commun.*, 2014, **50**, 4047-4049.
49. K. Epp, B. Bueken, B. J. Hofmann, M. Cokoja, K. Hemmer, D. De Vos and R. A. Fischer, *Catal. Sci. Technol.*, 2019, **9**, 6452-6459.
50. L. Ye, Y. Ying, D. Sun, Z. Zhang, L. Fei, Z. Wen, J. Qiao and H. Huang, *Angew. Chem. Int. Ed.*, 2020, **59**, 3244-3251.
51. X. Li and Q.-L. Zhu, *EnergyChem*, 2020, **2**, 100033.
52. Y. Liu, Y. Yang, Q. Sun, Z. Wang, B. Huang, Y. Dai, X. Qin and X. Zhang, *ACS Appl.*

*Mater. Interfaces*, 2013, **5**, 7654-7658.

View Article Online  
DOI: 10.1039/D4EE01748J

53. E. G. Percástegui and V. Jancik, *Coordin. Chem. Rev.*, 2020, **407**, 213165.
54. D. Yang, S. Zuo, H. Yang, Y. Zhou, Q. Lu and X. Wang, *Adv. Mater.*, 2022, **34**, e2107293.
55. X. Chen, D. Wang, Z. Wang, Y. Li, H. Zhu, X. Lu, W. Chen, H. Qiu and Q. Zhang, *Chem. Eng. J.*, 2021, **424**.
56. J. Gu, Y. Peng, T. Zhou, J. Ma, H. Pang and Y. Yamauchi, *Nano Res. Energy*, 2022, **1**, e9120009.
57. W. Han, X. Ma, J. Wang, F. Leng, C. Xie and H. L. Jiang, *J. Am. Chem. Soc.*, 2023, **145**, 9665-9671.
58. B. J. Burnett, P. M. Barron and W. Choe, *CrystEngComm*, 2012, **14**, 3839.
59. D. Chen, Z. Guo, B. Li and H. Xing, *New J. Chem.*, 2022, **46**, 16297-16302.
60. P. Deria, J. E. Mondloch, O. Karagiari, W. Bury, J. T. Hupp and O. K. Farha, *Chem. Soc. Rev.*, 2014, **43**, 5896-5912.
61. Y. T. Guntern, J. R. Pankhurst, J. Vavra, M. Mensi, V. Mantella, P. Schouwink and R. Buonsanti, *Angew. Chem. Int. Ed.*, 2019, **58**, 12632-12639.
62. Z. W. Huang, K. Q. Hu, X. B. Li, Z. N. Bin, Q. Y. Wu, Z. H. Zhang, Z. J. Guo, W. S. Wu, Z. F. Chai, L. Mei and W. Q. Shi, *J. Am. Chem. Soc.*, 2023, **145**, 18148-18159.
63. L. Wang, H. Fan and F. Bai, *MRS Bull.*, 2020, **45**, 49-56.
64. L. Wang, P. Jin, J. Huang, H. She and Q. Wang, *ACS Sustainable Chem. Eng.*, 2019, **7**, 15660-15670.
65. S. Wang and X. Wang, *Small*, 2015, **11**, 3097-3112.
66. Z. Wang, Q. Sun, B. Liu, Y. Kuang, A. Gulzar, F. He, S. Gai, P. Yang and J. Lin, *Coordin. Chem. Rev.*, 2021, **439**, 213945.
67. J. Chen, Y. Zhu and S. Kaskel, *Angew. Chem. Int. Ed.*, 2021, **60**, 5010-5035.
68. X. Zhang, M. C. Wasson, M. Shayan, E. K. Berdichevsky, J. Ricardo-Noordberg, Z. Singh, E. K. Papazyan, A. J. Castro, P. Marino, Z. Ajoyan, Z. Chen, T. Islamoglu, A. J. Howarth, Y. Liu, M. B. Majewski, M. J. Katz, J. E. Mondloch and O. K. Farha, *Coordin. Chem. Rev.*, 2021, **429**, 213615.
69. S. Mehrzad Sajjadinezhad, L. Boivin, K. Bouarab and P. D. Harvey, *Coordin. Chem. Rev.*, 2024, **510**, 215794.
70. F. Liu, I. Rincón, H. G. Baldoví, A. Dhakshinamoorthy, P. Horcajada, S. Rojas, S. Navalón and A. Fateeva, *Inorg. Chem. Front.*, 2024, **11**, 2212-2245.
71. Y. G. Gorbunova, Y. Y. Enakieva, M. V. Volostnykh, A. A. Sinelshchikova, I. A. Abdulaeva, K. P. Birin and A. Y. Tsivadze, *Russ. Chem. Rev.*, 2022, **91**, RCR5038.
72. P. D. Harvey, *J. Mater. Chem. C*, 2021, **9**, 16885-16910.
73. Q. Wang, Q. Gao, A. M. Al-Enizi, A. Nafady and S. Ma, *Inorg. Chem. Front.*, 2020, **7**, 300-339.
74. T. Xia, Y. Lin, W. Li and M. Ju, *Chinese Chem. Lett.*, 2021, **32**, 2975-2984.
75. Y. Zhao, L. Zheng, D. Jiang, W. Xia, X. Xu, Y. Yamauchi, J. Ge and J. Tang, *Small*, 2021, **17**, e2006590.
76. F. ZareKarizi, M. Joharian and A. Morsali, *J. Mater. Chem. A*, 2018, **6**, 19288-19329.
77. S. Yuan, J. S. Qin, L. Zou, Y. P. Chen, X. Wang, Q. Zhang and H. C. Zhou, *J. Am. Chem. Soc.*, 2016, **138**, 6636-6642.

78. R. Shimoni, Z. Shi, S. Binyamin, Y. Yang, I. Liberman, R. Ifraemov, S. Mukhopadhyay, L. Zhang and I. Hod, *Angew. Chem. Int. Ed.*, 2022, **61**, e202206085. View Article Online  
DOI: 10.1039/D4EE01748J
79. M. C. So, G. P. Wiederrecht, J. E. Mondloch, J. T. Hupp and O. K. Farha, *Chem. Commun.*, 2015, **51**, 3501-3510.
80. J. Wang, Y. Zhang, Y. Ma, J. Yin, Y. Wang and Z. Fan, *ACS Mater. Lett.*, 2022, **4**, 2058-2079.
81. P. Deria, J. Yu, R. P. Balaraman, J. Mashni and S. N. White, *Chem. Commun.*, 2016, **52**, 13031-13034.
82. B. Karadeniz, D. Zilic, I. Huskic, L. S. Germann, A. M. Fidelli, S. Muratovic, I. Loncaric, M. Etter, R. E. Dinnebier, D. Barisic, N. Cindro, T. Islamoglu, O. K. Farha, T. Friscic and K. Uzarevic, *J. Am. Chem. Soc.*, 2019, **141**, 19214-19220.
83. Y. Zhao, L. Jiang, L. Shanguan, L. Mi, A. Liu and S. Liu, *J. Mater. Chem. A*, 2018, **6**, 2828-2833.
84. S. Ali Akbar Razavi and A. Morsali, *Coordin. Chem. Rev.*, 2019, **399**, 213023.
85. X. Zhang, M. C. Wasson, M. Shayan, E. K. Berdichevsky, J. Ricardo-Noordberg, Z. Singh, E. K. Papazyan, A. J. Castro, P. Marino, Z. Ajoyan, Z. Chen, T. Islamoglu, A. J. Howarth, Y. Liu, M. B. Majewski, M. J. Katz, J. E. Mondloch and O. K. Farha, *Coordin. Chem. Rev.*, 2021, **429**, 213615.
86. T.-F. Liu, D. Feng, Y.-P. Chen, L. Zou, M. Bosch, S. Yuan, Z. Wei, S. Fordham, K. Wang and H.-C. Zhou, *J. Am. Chem. Soc.*, 2014, **137**, 413-419.
87. X. D. Zhang, S. Z. Hou, J. X. Wu and Z. Y. Gu, *Chem. Eur. J.*, 2020, **26**, 1604-1611.
88. L. Yang, P. Cai, L. Zhang, X. Xu, A. A. Yakovenko, Q. Wang, J. Pang, S. Yuan, X. Zou, N. Huang, Z. Huang and H.-C. Zhou, *J. Am. Chem. Soc.*, 2021, **143**, 12129-12137.
89. D.-J. Li, Y.-B. Tian, Q. Lin, J. Zhang and Z.-G. Gu, *ACS Appl. Mater. Interfaces*, 2022, **14**, 33548-33554.
90. K. Nisa, M. Saxena, I. A. Lone and R. Kumar, *Sustain. Energy Fuels*, 2023, **7**, 2774-2801.
91. J. Park, M. Xu, F. Li and H. C. Zhou, *J. Am. Chem. Soc.*, 2018, **140**, 5493-5499.
92. J. Zheng, M. Wu, F. Jiang, W. Su and M. Hong, *Chem. Sci.*, 2015, **6**, 3466-3470.
93. Q. Chen, S. Xian, X. Dong, Y. Liu, H. Wang, D. H. Olson, L. J. Williams, Y. Han, X. H. Bu and J. Li, *Chem. Commun.*, 2021, **60**, 10593-10597.
94. Z. Zhu, Z. Wang, Q. H. Li, Z. Ma, F. Wang and J. Zhang, *Dalton Trans.*, 2023, **52**, 4309-4314.
95. C. Xia, R. T. Guo, Z. X. Bi, Z. R. Zhang, C. F. Li and W. G. Pan, *Dalton Trans.*, 2023, **52**, 12742-12754.
96. Z. Xin, J. Liu, X. Wang, K. Shen, Z. Yuan, Y. Chen and Y. Q. Lan, *ACS Appl. Mater. Interfaces*, 2021, **13**, 54959-54966.
97. X. Xiong, Y. Zhao, R. Shi, W. Yin, Y. Zhao, G. I. N. Waterhouse and T. Zhang, *Sci. Bull.*, 2020, **65**, 987-994.
98. S. Yuan, J.-S. Qin, L. Zou, Y.-P. Chen, X. Wang, Q. Zhang and H.-C. Zhou, *J. Am. Chem. Soc.*, 2016, **138**, 6636-6642.
99. Z. Wang, Q. Sun, B. Liu, Y. Kuang, A. Gulzar, F. He, S. Gai, P. Yang and J. Lin, *Coordin. Chem. Rev.*, 2021, **439**, 213945.
100. Y. Wang, L. Feng, J. Pang, J. Li, N. Huang, G. S. Day, L. Cheng, H. F. Drake, Y. Wang,

- C. Lollar, J. Qin, Z. Gu, T. Lu, S. Yuan and H. C. Zhou, *Adv. Sci.*, 2019, **6**. View Article Online  
DOI: 10.1039/D4EE01748J
101. S. Kumar, M. A. Isaacs, R. Trofimovaite, L. Durndell, C. M. A. Parlett, R. E. Douthwaite, B. Coulson, M. C. R. Cockett, K. Wilson and A. F. Lee, *Appl. Catal. B: Environ.*, 2017, **209**, 394-404.
102. T. Lai, J. Wang, W. Xiong, H. Wang, M. Yang, T. Li, X. Kong, X. Zou, Y. Zhao, D. O'Hare and Y.-F. Song, *Chem. Eng. Sci.*, 2022, **257**, 117704.
103. L. Cheng, X. Yue, L. Wang, D. Zhang, P. Zhang, J. Fan and Q. Xiang, *Adv. Mater.*, 2021, **33**, e2105135.
104. A. A. Zhang, D. Si, H. Huang, L. Xie, Z. B. Fang, T. F. Liu and R. Cao, *Angew. Chem. Int. Ed.*, 2022, **61**, e202203955.
105. N. Heidary, M. Morency, D. Chartrand, K. H. Ly, R. Iftimie and N. Kornienko, *J. Am. Chem. Soc.*, 2020, **142**, 12382-12393.
106. B. Petrovic, M. Gorbounov and S. Masoudi Soltani, *Micropor. Mesopor. Mater.*, 2021, **312**, 110751..
107. J. Liu, L. Chen, H. Cui, J. Zhang, L. Zhang and C.-Y. Su, *Chem. Soc. Rev.*, 2014, **43**, 6011-6061.
108. M. Cheng, P. Yan, X. Zheng, B. Gao, X. Yan, G. Zhang, X. Cui and Q. Xu, *Chem. Eur. J.*, 2023, **29**, e202302395.
109. G. Singh, J. Lee, A. Karakoti, R. Bahadur, J. Yi, D. Zhao, K. AlBahily and A. Vinu, *Chem. Soc. Rev.*, 2020, **49**, 4360-4404.
110. J.-S. Qin, S. Yuan, Q. Wang, A. Alsalme and H.-C. Zhou, *J. Mater. Chem. A*, 2017, **5**, 4280-4291.
111. Q. Wu, J. Wang, Z. Wang, Y. Xu, Z. Xing, X. Zhang, Y. Guan, G. Liao and X. Li, *J. Mater. Chem. A*, 2020, **8**, 13685-13693.
112. K. Yu, D.-I. Won, W. I. Lee and W.-S. Ahn, *Korean J. Chem. Eng.*, 2021, **38**, 653-673.
113. Z.-B. Fang, T.-T. Liu, J. Liu, S. Jin, X.-P. Wu, X.-Q. Gong, K. Wang, Q. Yin, T.-F. Liu, R. Cao and H.-C. Zhou, *J. Am. Chem. Soc.*, 2020, **142**, 12515-12523.
114. M. Cheng, B. Gao, X. Zheng, W. Wu, W. Kong, P. Yan, Z. Wang, B. An, Y. Zhang, Q. Li and Q. Xu, *Appl. Catal. B: Environ.*, 2024, **353**, 124097.
115. S. M. Pratik, L. Gagliardi and C. J. Cramer, *J. Phys. Chem. C*, 2019, **124**, 1878-1887.
116. M. R. Smith, C. B. Martin, S. Arumuganainar, A. Gilman, B. E. Koel and M. L. Sarazen, *Angew. Chem. Int. Ed.*, 2023, **62**, e202218208.
117. P. J. Chmielewski and L. Latos-Grażyński, *Coordin. Chem. Rev.*, 2005, **249**, 2510-2533.
118. C. Wang, X.-M. Liu, M. Zhang, Y. Geng, L. Zhao, Y.-G. Li and Z.-M. Su, *ACS Sustainable Chem. Eng.*, 2019, **7**, 14102-14110.
119. S. Xie, C. Deng, Q. Huang, C. Zhang, C. Chen, J. Zhao and H. Sheng, *Angew. Chem. Int. Ed.*, 2023, **62**, e202216717.
120. M. Zhou, Z. Qu, J. Zhang, H. Jiang, Z. Tang and R. Chen, *Chem. Commun.*, 2024, **60**, 3170-3173.
121. H. Che, C. Liu, G. Che, G. Liao, H. Dong, C. Li, N. Song and C. Li, *Nano Energy*, 2020, **67**, 104273.
122. E. Roduner, *Chem. Soc. Rev.*, 2014, **43**, 8226-8239..
123. G. Liao, J. Fang, Q. Li, S. Li, Z. Xu and B. Fang, *Nanoscale*, 2019, **11**, 7062-7096.
124. Z. Jiang, Y. Liu, T. Jing, B. Huang, Z. Wang, X. Zhang, X. Qin and Y. Dai, *Appl. Catal.*

- B: Environ.*, 2017, **200**, 230-236.
125. R.-t. Guo, C. Xia and W.-g. Pan, *J. Chem. Educ.*, 2023, **100**, 1621-1626.
126. H. Li, Y. Jiang, X. Li, K. Davey, Y. Zheng, Y. Jiao and S. Z. Qiao, *J. Am. Chem. Soc.*, 2023, **145**, 14335-14344.
127. N. Sadeghi, S. Sharifnia and M. Sheikh Arabi, *J. CO<sub>2</sub> Util.*, 2016, **16**, 450-457.
128. X. J. Kong, T. He, J. Zhou, C. Zhao, T. C. Li, X. Q. Wu, K. Wang and J. R. Li, *Small*, 2021, **17**.
129. S. Bai, Z. Wang, L. Tan, G. I. N. Waterhouse, Y. Zhao and Y.-F. Song, *Ind. Eng. Chem. Res.*, 2020, **59**, 5848-5857.
130. P. Deria, J. Yu, R. P. Balaraman, J. Mashni and S. N. White, *Chem. Commun.*, 2016, **52**, 13031-13034.
131. H. Zhang, J. Wei, J. Dong, G. Liu, L. Shi, P. An, G. Zhao, J. Kong, X. Wang, X. Meng, J. Zhang and J. Ye, *Angew. Chem. Int. Ed.*, 2016, **55**, 14310-14314.
132. Z.-W. Huang, K.-Q. Hu, X.-B. Li, Z.-N. Bin, Q.-Y. Wu, Z.-H. Zhang, Z.-J. Guo, W.-S. Wu, Z.-F. Chai, L. Mei and W.-Q. Shi, *J. Am. Chem. Soc.*, 2023, **145**, 18148-18159.
133. S. Xie, Y. Li, B. Sheng, W. Zhang, W. Wang, C. Chen, J. Li, H. Sheng and J. Zhao, *Appl. Catal. B: Environ.*, 2022, **310**, 121320.
134. J. Liang, H. Yu, J. Shi, B. Li, L. Wu and M. Wang, *Adv. Mater.*, 2023, **35**, 2209814.
135. C. Zheng, X. Qiu, J. Han, Y. Wu and S. Liu, *ACS Appl. Mater. Interfaces*, 2019, **11**, 42243-42249.
136. L. Tayebi, R. Rahimi and A. R. Akbarzadeh, *ACS Omega*, 2022, **7**, 40869-40881.
137. T. Tang, Z. Wang and J. Guan, *Adv. Funct. Mater.*, 2022, **32**, 2111504.
138. K. Liu, Y. Liao, P. Wang, X. Fang, J. Zhu, G. Liao and X. Xu, *Nanoscale*, 2024, DOI: 10.1039/D4NR01409J.
139. T. Rhauderwiek, S. Waitschat, S. Wuttke, H. Reinsch, T. Bein and N. Stock, *Inorg. Chem.*, 2016, **55**, 5312-5319.
140. S. Senthilkumar, R. Goswami, N. L. Obasi and S. Neogi, *ACS Sustainable Chem. Eng.*, 2017, **5**, 11307-11315.
141. G. Zhou, Y. Wang and Z. Huang, *Chem Catal.*, 2022, **2**, 3304-3319.
142. J. Liang, H. Yu, J. Shi, B. Li, L. Wu and M. Wang, *Adv. Mater.*, 2023, **35**, e2209814.
143. Z. Liang, H. Y. Wang, H. Zheng, W. Zhang and R. Cao, *Chem. Soc. Rev.*, 2021, **50**, 2540-2581.
144. J. Liu, Y.-Z. Fan, X. Li, Z. Wei, Y.-W. Xu, L. Zhang and C.-Y. Su, *Appl. Catal. B: Environ.*, 2018, **231**, 173-181.
145. J.-X. Wu, S.-Z. Hou, X.-D. Zhang, M. Xu, H.-F. Yang, P.-S. Cao and Z.-Y. Gu, *Chem. Sci.*, 2019, **10**, 2199-2205.
146. X. Li, L. Wang, Y. Xing and W. Su, *Sustain. Energy Fuels*, 2022, **6**, 3516-3526.
147. Y.-L. Dong, Z.-Y. Jing, Q.-J. Wu, Z.-A. Chen, Y.-B. Huang and R. Cao, *J. Mater. Chem. A*, 2023, **11**, 8739-8746.
148. I. Hod, M. D. Sampson, P. Deria, C. P. Kubiak, O. K. Farha and J. T. Hupp, *ACS Catal.*, 2015, **5**, 6302-6309.
149. R. Li, W. Zhang and K. Zhou, *Adv. Mater.*, 2018, **30**, e1705512.
150. C. Ma, Z. Wang, J. Li, M. Mu and X. Yin, *Electrochim. Acta*, 2023, **463**, 142774.
151. D. Yang, S. Zuo, H. Yang, Y. Zhou, Q. Lu and X. Wang, *Adv. Mater.*, 2022, **34**,

2107293.

[View Article Online](#)  
DOI: 10.1039/D4EE01748J

152. H.-L. Zhu, H.-Y. Chen, Y.-X. Han, Z.-H. Zhao, P.-Q. Liao and X.-M. Chen, *J. Am. Chem. Soc.*, 2022, **144**, 13319-13326.
153. H. Yang, S. Li and Q. Xu, *Chinese J. Catal.*, 2023, **48**, 32-65.
154. X. Xie, X. Zhang, M. Xie, L. Xiong, H. Sun, Y. Lu, Q. Mu, M. H. Rummeli, J. Xu, S. Li, J. Zhong, Z. Deng, B. Ma, T. Cheng, W. A. Goddard and Y. Peng, *Nat. Commun.*, 2022, **13**, 63.
155. S. Xie, Y. Li, B. Sheng, W. Zhang, W. Wang, C. Chen, J. Li, H. Sheng and J. Zhao, *Appl. Catal. B: Environ.*, 2022, **310**, 121320.
156. J. Li, H. Shen, C. Ma, H. Zhang, P. Luo, J. Chen, M. Mu and X. Yin, *Electrochim. Acta*, 2023, **443**, 123684.
157. Y. Zhou, L. Zheng, D. Yang, H. Yang, Q. Lu, Q. Zhang, L. Gu and X. Wang, *Small Methods*, 2021, **5**, e2000991.
158. N. Kornienko, Y. Zhao, C. S. Kley, C. Zhu, D. Kim, S. Lin, C. J. Chang, O. M. Yaghi and P. Yang, *J. Am. Chem. Soc.*, 2015, **137**, 14129-14135.
159. J. X. Wu, S. Z. Hou, X. D. Zhang, M. Xu, H. F. Yang, P. S. Cao and Z. Y. Gu, *Chem. Sci.*, 2019, **10**, 2199-2205.